

# Is AGN feedback necessary to form red elliptical galaxies?

A. Khalatyan<sup>\*</sup>, A. Cattaneo<sup>†</sup>, M. Schramm, S. Gottlöber, M. Steinmetz, L. Wisotzki

*Astrophysikalisches Institut Potsdam, An der Sternwarte 16, 14482 Potsdam, Germany*

<sup>\*</sup>*akhalatyan@aip.de*, <sup>†</sup>*acattaneo@aip.de*

26 October 2018

## ABSTRACT

We have used the smoothed particle hydrodynamics (SPH) code GADGET-2 to simulate the formation of an elliptical galaxy in a group-size cosmological dark matter halo with mass  $M_{\text{halo}} \simeq 3 \times 10^{12} h^{-1} M_{\odot}$  at  $z = 0$ . The use of a stellar population synthesis model has allowed us to compute magnitudes, colours and surface brightness profiles. We have included a model to follow the growth of a central black hole and we have compared the results of simulations with and without feedback from active galactic nuclei (AGNs). We have studied the interplay between cold gas accretion and merging in the development of galactic morphologies, the link between colour and morphology evolution, the effect of AGN feedback on the photometry of early type galaxies, the redshift evolution in the properties of quasar hosts, and the impact of AGN winds on the chemical enrichment of the intergalactic medium (IGM).

We have found that the early phases of galaxy formation are driven by the accretion of cold filamentary flows, which form a disc galaxy at the centre of the dark matter halo. Disc star formation rates in this mode of galaxy growth are about as high as the peak star formation rates attained at a later epoch in galaxy mergers. When the dark matter halo is sufficiently massive to support the propagation of a stable shock, the gas in the filaments is heated to the virial temperature, cold accretion is shut down, and the star formation rate begins to decline.

Mergers transform the spiral galaxy into an elliptical one, but they also reactivate star formation by bringing gas into the galaxy. Without a mechanism that removes gas from the merger remnants, the galaxy ends up with blue colours, that are atypical for its elliptical morphology. We have demonstrated that AGN feedback can solve this problem even with a fairly low heating efficiency. Our simulations support a picture where AGN feedback is important for quenching star formation in the remnant of wet mergers and for moving them to the red sequence. This picture is consistent with recent observational results, which suggest that AGN hosts are galaxies in migration from the blue cloud to the red sequence on the colour – magnitude diagram. However, we have also seen a transition in the properties of AGN hosts from blue and star-forming at  $z \sim 2$  to mainly red and dead at  $z \sim 0$ . Ongoing merging is the primary but not the only triggering mechanism for luminous AGN activity.

Quenching by AGNs is only effective after the cold filaments have dried out, since otherwise the galaxy is constantly replenished with gas. AGN feedback also contributes to raising the entropy of the hot IGM by removing low entropy tails vulnerable to developing cooling flows. We have also demonstrated that AGN winds are potentially important for the metal enrichment of the IGM a high redshift.

**Key words:** galaxies: formation, evolution, active, cooling flows, intergalactic medium

## 1 INTRODUCTION

The most massive galaxies are elliptical. Their colours and spectra are clearly separated from those of blue spirals (e.g. Kauffmann et al. 2003a, 2004; Baldry et al. 2006). Most of their light comes from old stellar populations (Thomas et al.

2005). Little or no star formation is presently going on in these galaxies (Kauffmann et al. 2003a, 2004).

Elliptical galaxies also host the most massive black holes. The relations that link the black hole mass to bulge properties such as luminosity, velocity dispersion

and mass (Magorrian et al. 1998; Ferrarese & Merritt 2000; Tremaine et al. 2002; Marconi & Hunt 2003; Häring & Rix 2004) point to an intimate link between the growth of black holes and the formation of spheroids, which is also seen in their coevolution (Cattaneo & Bernardi 2003; Hopkins et al. 2007a). A number of studies have suggested that the relation between black hole mass and bulge velocity dispersion arises because black holes grow until they are sufficiently massive to blow away the gas that feeds their accretion (Silk & Rees 1998; Fabian 1999; King 2003; Di Matteo et al. 2005; Murray et al. 2005; Springel et al. 2005a; Fabian et al. 2007). This proposal is attractive because it also provides a mechanism for terminating star formation after a phase of rapid black hole growth (e.g. Springel et al. 2005a; Hopkins et al. 2007a,b).

Previous studies of the role of AGNs in the formation of red elliptical galaxies have concentrated on two opposite scenarios. The first one links AGN feedback to the growth of supermassive black holes in galaxy mergers (e.g. Springel et al. 2005a,b; Hopkins et al. 2005, 2007a,b,c). The second one connects the colour bimodality to the shutdown of cold gas accretion in massive haloes (Kereš et al. 2005; Dekel & Birnboim 2006; Bower et al. 2006; Cattaneo et al. 2006, 2007). In the second picture, AGNs play a ‘maintenance’ role by coupling to the hot IGM and therefore by preventing it from cooling (Best et al. 2006; Cattaneo et al. 2006; Croton et al. 2006; Dunn & Fabian 2006; Fabian et al. 2006; Rafferty et al. 2006; Cattaneo & Teyssier 2007). Both pictures reveal physical aspects of the black hole – galaxy interaction, but neither of them tells the whole story when it is considered in isolation. This is our motivation for studying black hole accretion and feedback in cosmological simulations, where we do not decide for the model at what stages of the formation of galaxies black holes should play a role.

Our first goal is to establish if AGN feedback is really necessary to form red ellipticals (see e.g. Birnboim et al. 2007; Khochfar & Ostriker 2007; Naab et al. 2007). Our second goal is to explore the link between star formation and morphology evolution. We want to study how mergers, AGNs and the thermal evolution of the IGM contribute to the development of the colour – morphology relation. We are also interested in the mechanisms that activate black hole accretion and in the role of AGN winds in the metal enrichment of the IGM.

We have addressed these questions by simulating the galaxy formation process in a dark matter halo that we have chosen to be massive enough to form an  $M_*$  elliptical galaxy ( $M_{\text{halo}} \simeq 3 \times 10^{12} h^{-1} M_{\odot}$ ) without being so massive as to make the simulations computationally prohibitive.

We have used the GADGET-2 SPH code (Springel 2005) to integrate the equations of motions for the dark matter and the baryons. Sub-grid physics (radiative cooling, two-phase structure of the ISM, star formation and supernovae) are followed with the model described by Springel & Hernquist (2003). The model for black hole accretion and feedback is the same as in Springel et al. (2005a). The Bruzual & Charlot (2003) stellar population synthesis model has been used for computing magnitudes, colours and surface brightness profiles, which we compare in simulations with and without AGN feedback. While the model of black accretion and feedback that we have used has already been employed by other researchers in

simulation of isolated mergers (e.g. Springel et al. 2005b; Hopkins et al. 2005; Cuadra et al. 2006) and cosmological simulations (Li et al. 2007), our work differentiates itself from previous studies in two respects. The first is that it uses high resolution cosmological simulations to investigate galaxy formation in a *group* environment. The second is the questions that it addresses, namely the interplay between cold flows and mergers in the development of galactic morphologies, the link between colour and morphology evolution, the redshift evolution in the properties of quasar hosts, the impact of AGN winds on the chemical enrichment of the intergalactic medium, and the effect of AGN feedback on the evolution of the photometric properties of early type galaxies. The study of the latter has been made possible by using a method where not only have we directly analysed the simulation outputs, but we have also used them to generate virtual astronomical data, which we have then analysed with standard observational analysis procedures.

The plan of the paper is as follows. In Section 2 we describe how the simulations are set up both in terms of the physical model and of its numerical implementation. Section 3 outlines the methods used to analyse the outputs of the simulations. Section 4 and 5 present the formation and the evolution of the central galaxy in the simulations respectively without and with AGN feedback. Section 6 discusses the effects of black hole heating on the thermal evolution of the IGM. Section 7 demonstrates the potential important of AGN winds for the early metal enrichment of the IGM. Section 8 summarises and discusses the main conclusions of this work.

## 2 THE SIMULATIONS

### 2.1 Initial conditions and numerical parameters

Using the mass refinement technique described by Klypin et al. (2001) (see also Navarro & Benz 1991; Navarro & Steinmetz 1997), we have simulated the formation of an individual elliptical galaxy within a dark matter halo selected for resimulation from a periodic computational box of side-length  $L = 50 h^{-1} \text{Mpc}$ .

To construct suitable initial conditions, we have first created a random realization with  $N = 2048^3$  particles of a concordance  $\Lambda$ CDM Universe ( $\Omega_m = 0.3$ ,  $\Omega_\Lambda = 0.7$ ,  $\Omega_b = 0.045$ , and  $h \equiv H_0/100 \text{ km s}^{-1} = 0.7$  for the Hubble constant). The initial matter power spectrum has been calculated using numerical results kindly provided by W. Hu, and it has been normalized to  $\sigma_8 = 0.9$ . Although  $\sigma_8 = 0.9$  is not what is currently favored by CMB observations, in the both Concordance and WMAP-3 realizations of the Universe it is possible to find galaxy with the same properties as we have presented. The differences are visible in a statistical sense, but not for a single object. Therefore our choice of  $\sigma_8$  has no bearing on our conclusions. The initial displacements and velocities of the particles have been calculated using all waves ranging from the fundamental mode  $k = 2\pi/L$  to the Nyquist frequency  $k_{ny} = 2\pi/L \times N^{1/3}/2$ . To produce initial conditions at lower mass resolution, we have randomly selected one in every  $8^n$  (where  $n=0, 1, 2, 3, 4, 5$ ) neighbouring particles, assigning to this particle the mass of all the  $8^n$  particles but keeping the position and velocity of the

selected particle. This procedure allows reducing the mass resolution without reducing the small-scale power. By this multiple mass technique one can get initial conditions of the same realization with different resolutions (e.g.  $2048^3$ ,  $1024^3$ ,  $512^3$  equivalent particle numbers), from which one can resimulate exactly the same objects, but with different resolutions.

The initial condition with a resolution of  $512^3$  particles has been evolved from  $z = 50$  to  $z = 0$  in a simulation with dark matter only presented in Maulbetsch et al. (2007). The halo finder used to identify dark matter haloes at  $z = 0$  is a new MPI+OpenMP version of the Bound Density Maxima (BDM) algorithm originally introduced by Klypin et al. (1999). This algorithm allows to detect isolated or “parent” haloes (self-bound structures not contained within larger ones) as well as subhaloes (self-bound structures contained within larger ones).

From the halo catalogue identified with the procedure, we have selected for resimulation a dark matter halo with  $M_{\text{halo}} \simeq 3.2 \times 10^{12} h^{-1} M_{\odot}$ . We have considered a sphere of radius  $R = 1.5 h^{-1} \text{Mpc}$  centred on this halo and we have used an equivalent resolution of  $1024^3$  particles for the low-mass particles inside  $R$ . Using several layers of particles with progressively increasing masses around the “region of interest” ensures that the resimulated halo evolves in the proper cosmological environment and with the right gravitational tidal fields while avoiding large jumps in mass resolution. The region of interest is much bigger than the virial radius of the selected halo to avoid the penetration of low-resolution massive particles into the resimulated object. In addition, we have not detected any intrusion of massive particles in the region of interest during the whole simulation.

Finally, we have assumed  $\Omega_b = 0.045$  and we have splitted the high-resolution particles into dark matter and gas particles. For dark matter particles we have achieved a mass resolution of  $M_p^{\text{DM}} \simeq 8.2 \times 10^6 h^{-1} M_{\odot}$ , while initially all baryons are in gas particles with mass  $M_p^{\text{gas}} = 1.48 \times 10^6 h^{-1} M_{\odot}$ .

Power et al. (2003) give a simple criterion for the gravitational softening length  $\varepsilon$  necessary in N-body simulations,  $\varepsilon \gtrsim r_{\text{vir}} / \sqrt{N_{\text{vir}}}$ , where  $r_{\text{vir}}$  and  $N_{\text{vir}}$  are the virial radius and the number of expected particles within it. They find that even a larger softening length keeps the central density profile unaffected. At  $z = 0$ , our resimulated halo has virial radius  $r_{\text{vir}} \sim 300 h^{-1} \text{kpc}$  and virial mass  $M_{\text{halo}} \simeq 3.2 \times 10^{12} h^{-1} M_{\odot}$ . Therefore, for the dark matter we have used a gravitational softening length equal to the maximum between  $0.6 \text{kpc}$  physical, which gives the gravitational softening length at high  $z$ , and  $3 h^{-1} \text{kpc}$  comoving, which gives the gravitational softening length at low  $z$ . The transition is at  $z = 4$ . After  $z = 4$ , the force resolution is kept constant in comoving coordinates:  $3 h^{-1} \text{kpc}$  for the dark matter,  $2 h^{-1} \text{kpc}$  for the gas and the stars, and  $1 h^{-1} \text{kpc}$  for the black hole. For the SPH calculations we have used  $40 \pm 1$  neighbours and we have imposed a minimum smoothing length equal to  $0.75\varepsilon$ .

We have performed two different simulations, with and without black hole (see Sections 2.3 and 2.4). The typical CPU time for a simulation was  $\sim 15$  CPU days on a SGI ALTIX machine with 64 processors.

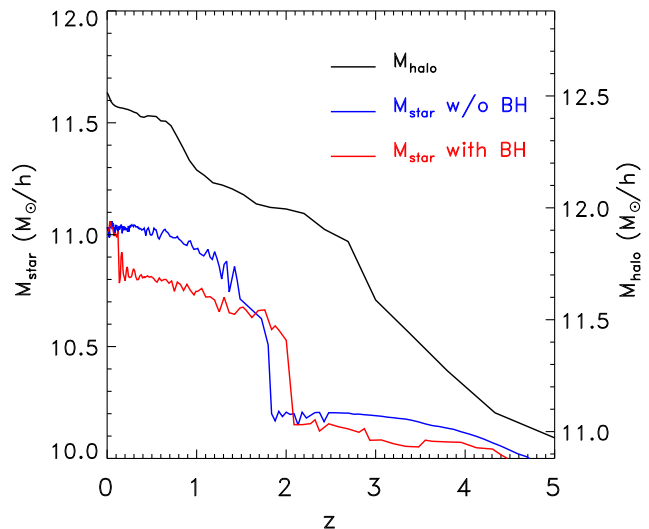


**Figure 1.** The growth of the stellar mass of the central galaxy and of the virial mass of the dark matter halo. The stellar mass shown in blue (red) is the one in the simulation without (with) AGN feedback. The halo mass (black) is essentially identical in the two simulations. The choice of different  $y$ -axes for the stellar mass (left) and the dark matter mass (right) is such that the curves for  $M_{\text{star}}$  and  $M_{\text{halo}}$  would overlap if  $M_{\text{star}} = f_b M_{\text{halo}}$ , where  $f_b \simeq 0.15$  is the assumed cosmic baryonic fraction.

## 2.2 Hydrodynamics, cooling and star formation

Our initial conditions have been evolved to  $z \sim 0$  with an updated version of the parallel TreePM-SPH hybrid code GADGET-2 (Springel et al. 2001). The code uses an entropy-conserving formulation of SPH (Springel & Hernquist 2002) which alleviates problems due to numerical over-cooling. The code also employs a new algorithm based on the TreePM method for the N-body calculations which speeds up the gravitational force computation significantly compared with a pure tree algorithm. Radiative cooling is computed as in Katz et al. (1996) assuming an optically thin primordial mix of hydrogen and helium. Photoionisation by an external uniform UV background is computed with the model by Haardt & Madau (1996).

The physics of star formation is treated with a subresolution model in which the gas of the interstellar medium (ISM) is described as a two phase medium of hot and cold gas (Yepes et al. 1997; Springel & Hernquist 2003; McKee & Ostriker 1977). Cold gas clouds are generated due to cooling and are the material out of which stars can be formed in regions that are sufficiently dense. Supernova feedback heats the hot phase of the ISM and evaporates cold clouds, thereby establishing a self-regulation cycle for star formation. The heat input due the supernovae also leads to a net pressurisation of the ISM, such that its effective equation of state becomes stiffer than isothermal. This stabilises the dense star forming gas in galaxies against further gravitational collapse, and allows converged numerical results for star formation even at moderate resolution.



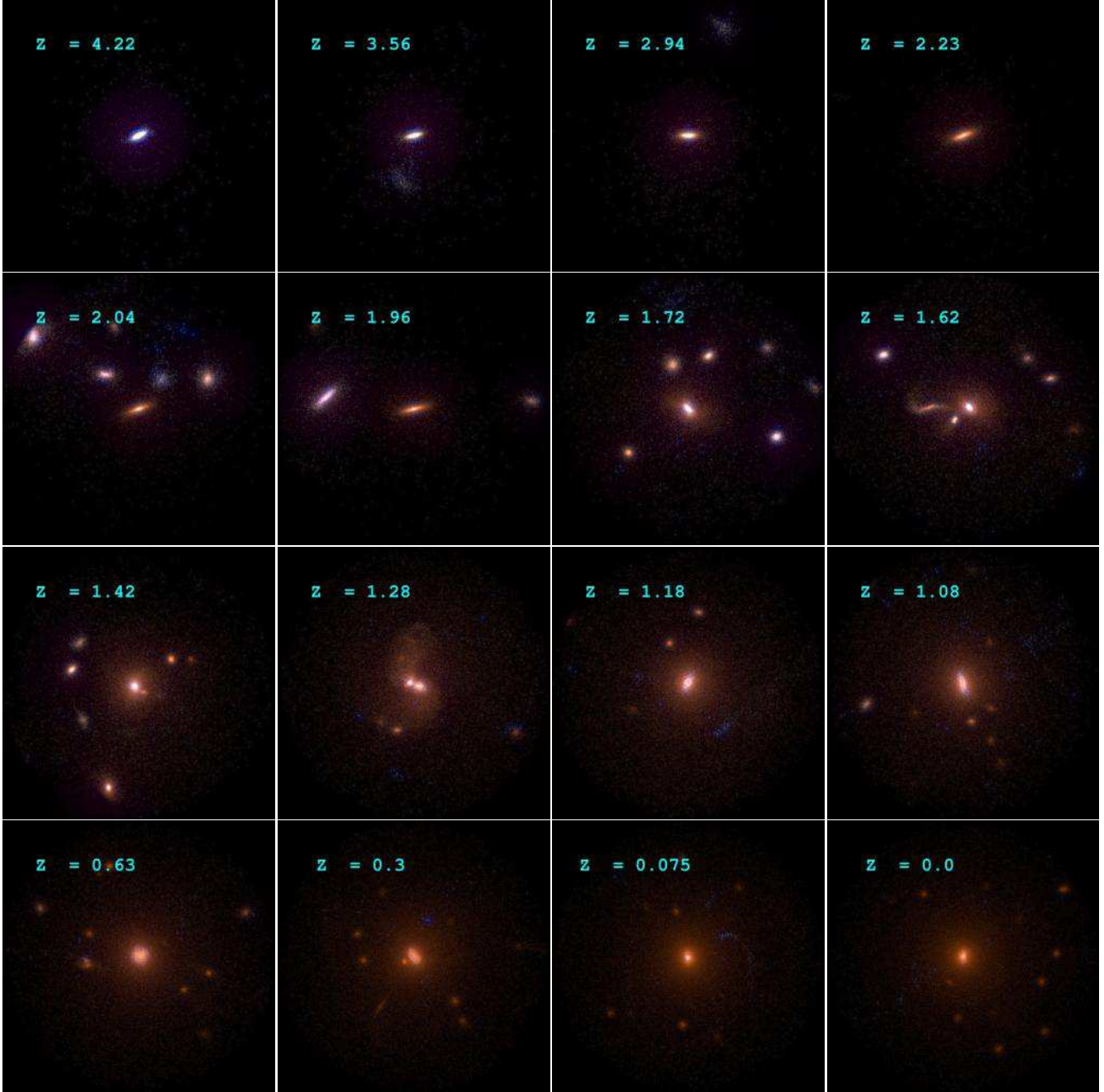


**Figure 2.** The simulation without AGN feedback. Each panel shows a composite UBV image of an  $100 \times 100 h^{-2} \text{ kpc}^2$  field. Composite UBV images have been generated by combining  $U$ ,  $B$  and  $V$  band .FITS images with the *STIFF* software by E. Bertin. *STIFF* makes composite colour images by mapping the  $VBU$  bands to the  $RGB$  colour channels. The snapshots have been selected to illustrate the key moments in the evolution of the central galaxy. At  $z \simeq 2.04 - 4.22$ , the galaxy has the characteristic aspect of a nearly edge-on spiral. During the fly-by at  $z \simeq 3.56$ , a small satellite is tidally disrupted and its debris are accreted by the central galaxy. The galaxy is transformed into an elliptical by a major merger at  $z \simeq 1.72$  followed by a second major merger at  $z \simeq 1.28$ . The visual morphology at  $z \lesssim 1$  is consistent with that of an E+A type object (a red elliptical with a central blue light excess).

When the SPH density exceeds the star formation threshold  $\rho_{\text{th}}$ , the ISM splits into two phases: a cold phase, made of star-forming clouds, and a hot phase, made of the tenuous gas that fills the space between the clouds. The two phases are in pressure equilibrium. They exchange mass and energy via cooling, supernova explosions and evaporation of clouds by the hot phase. In our simulations,  $\rho_{\text{th}}$  corresponds to  $n_{\text{H}} \simeq 0.25 h^2 \text{ cm}^{-3}$ . The cold phase makes stars on the

timescale  $t_{\star} = t_0^* (\rho / \rho_{\text{th}})^{-1/2}$ , where  $t_0^* = 2.1 \text{ Gy}^1$ . These values are chosen to reproduce the Kennicutt (1998) law.

Supernova feedback and metal enrichment take place

<sup>1</sup> From a numerical point of view, each gas particle can spawn two generations of stars. Therefore, the mass of a stellar particle is half of the initial gas-particle mass.

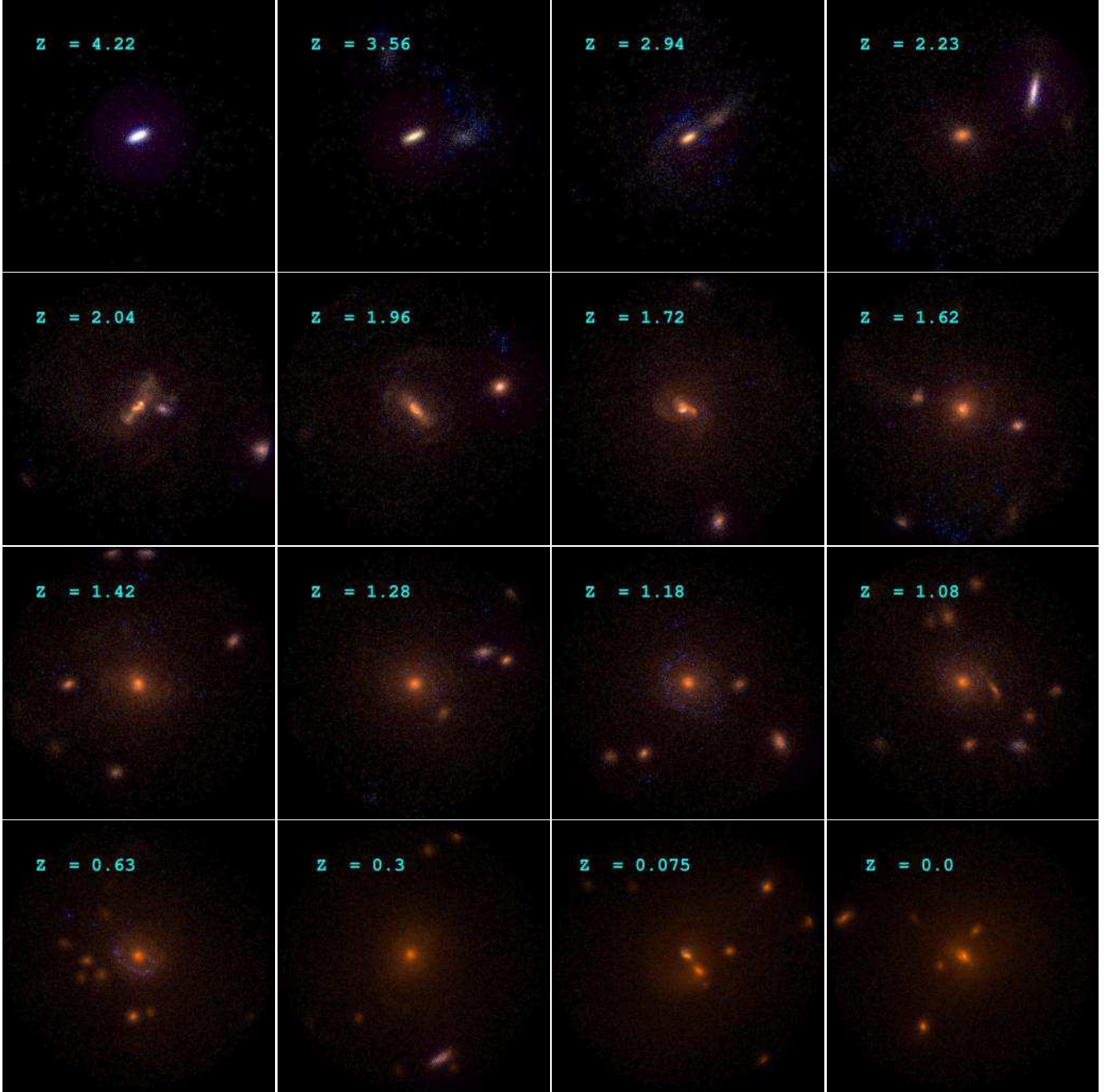


**Figure 3.** The same as Fig. 2 but for the simulation with AGN feedback. The galaxy experienced a major merger associated with luminous AGN activity ( $L_{\text{AGN}} \sim L_{\text{Edd}}$ ,  $M_B \sim -22.6$ ) at  $z \simeq 2.04$  followed by another major merger at  $z \simeq 1.72$  and a minor merger at  $z \simeq 1.08 - 1.18$ . Both produce Seyfert activity at the level of  $M_B \sim -21.7$ . The accretion of a tidal feature at  $z \simeq 0.63$  fuels another flare of black hole activity, which is less powerful than the previous ones ( $M_B \sim -21$ ) but removes all the cold gas that remains in the galaxy causing its transition to the red sequence. A major merger at  $z \simeq 0.075$  causes the galaxy to become temporarily bluer in the central region. However star formation is quenched by the activation of an AGN ( $L_{\text{AGN}} \sim L_{\text{Edd}}$ ,  $M_B \sim -23$ ) before any substantial stellar mass is formed. At  $z \sim 0$  the galaxy has the visual morphology, the photometric properties and the colours of a red elliptical. As the purpose of these images is to show the host galaxy evolution, we have assumed that the AGN is obscured (type 2) at all observing times.

instantaneously whenever stars are formed. For each  $1 M_{\odot}$  of stars formed,  $0.02 M_{\odot}$  of metals are distributed to neighbouring gas particles. Because we have used a fixed (primordial) metallicity for computing cooling, there is no issue of using the metallicity of individual particles or smoothing with the SPH kernel. Stars have the metallicity of the gas out of which they are formed. As in Springel & Hernquist

(2003), we adopt a Salpeter (power law) stellar initial mass function (IMF) with a slope of  $-1.3$ , a minimum stellar mass of  $0.1 M_{\odot}$ , and a maximum stellar mass of  $40 M_{\odot}$ , and we assume that a fraction  $\beta_{\text{SN}} = 0.1$  of the mass that forms stars is returned to the hot phase as supernova ejecta with  $T_{\text{SN}} = 10^8$  K. The mass evaporated from the cold phase of the ISM is larger than this fraction by a factor



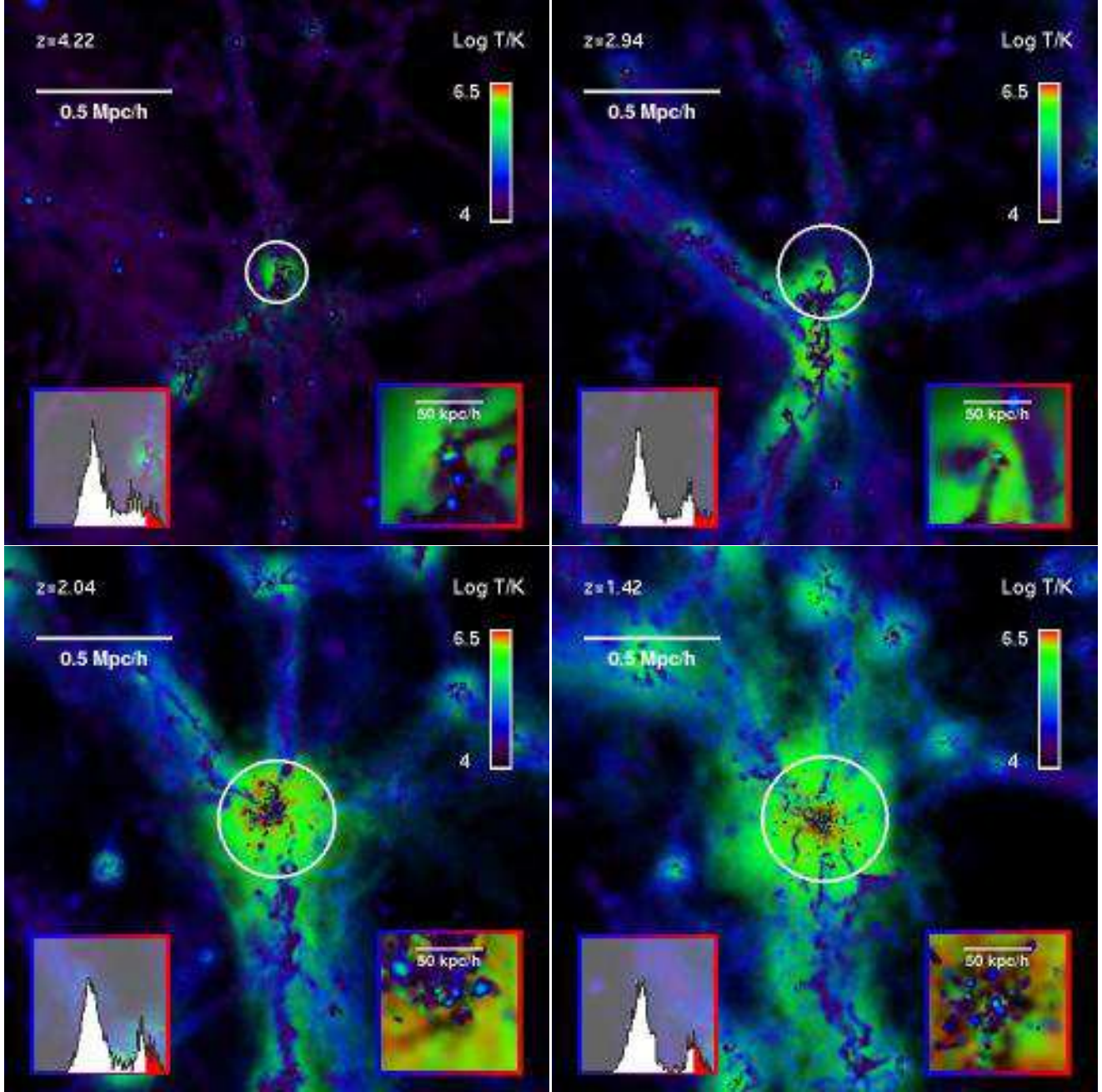


**Figure 4.** Density and temperature structure of the IGM in the simulation without AGN feedback (continues on the next page). Each image shows a cube of  $(2h^{-1} \text{ Mpc})^3$  centred on the central galaxy. Intensity shows density while hue shows temperature. The white circle around the central galaxy shows the virial radius of the dark matter halo. The little subpanel in the lower right corner of each image shows an enlargement of the central region. The colour coding is the same as for the large scale image. The histogram on each panel shows the density distribution of the gas in the  $(2h^{-1} \text{ Mpc})^3$  cube. It spans a logarithmic number density range from  $10^{-10} h^2 \text{ cm}^3$  to  $10 h^2 \text{ cm}^3$ . The presence of a cold dense phase and a hot dilute phase is clearly visible. The red part of the histogram shows the gas with density greater than the star formation threshold  $n_H \sim 0.19 h^2 \text{ cm}^3$ . The histogram, therefore, shows the proportion between the masses of the hot IGM, the cold IGM and the ISM, which corresponds to the red part of the histogram. At high redshift the gas is cold and flows onto the central galaxy in filamentary streams ( $z \simeq 4.22$ ). At  $z \sim 2.04 - 2.94$ , a halo of hot gas has formed inside the virial radius. At  $z \sim 1.08 - 1.42$ , the cold filaments fragment and dissolve. By  $z \lesssim 0.30$  there is little cold gas inside the virial radius.

of  $A = A_0(\rho/\rho_{\text{th}})^{-4/5}$ , where  $A_0 = 10^3$ , so that the hot phase's equilibrium temperature at  $\rho_{\text{th}}$ ,  $T_{\text{SN}}/A_0$ , is around the maximum of the cooling function.

### 2.3 Black hole accretion and feedback

The main difficulty of inserting a supermassive black hole in a cosmological hydrodynamic simulation is that we can only follow its dynamics adequately when  $M_{\text{bh}} \gg M_{\text{p}}^{\text{gas}}$ . This occurs because the black hole absorbs the momentum

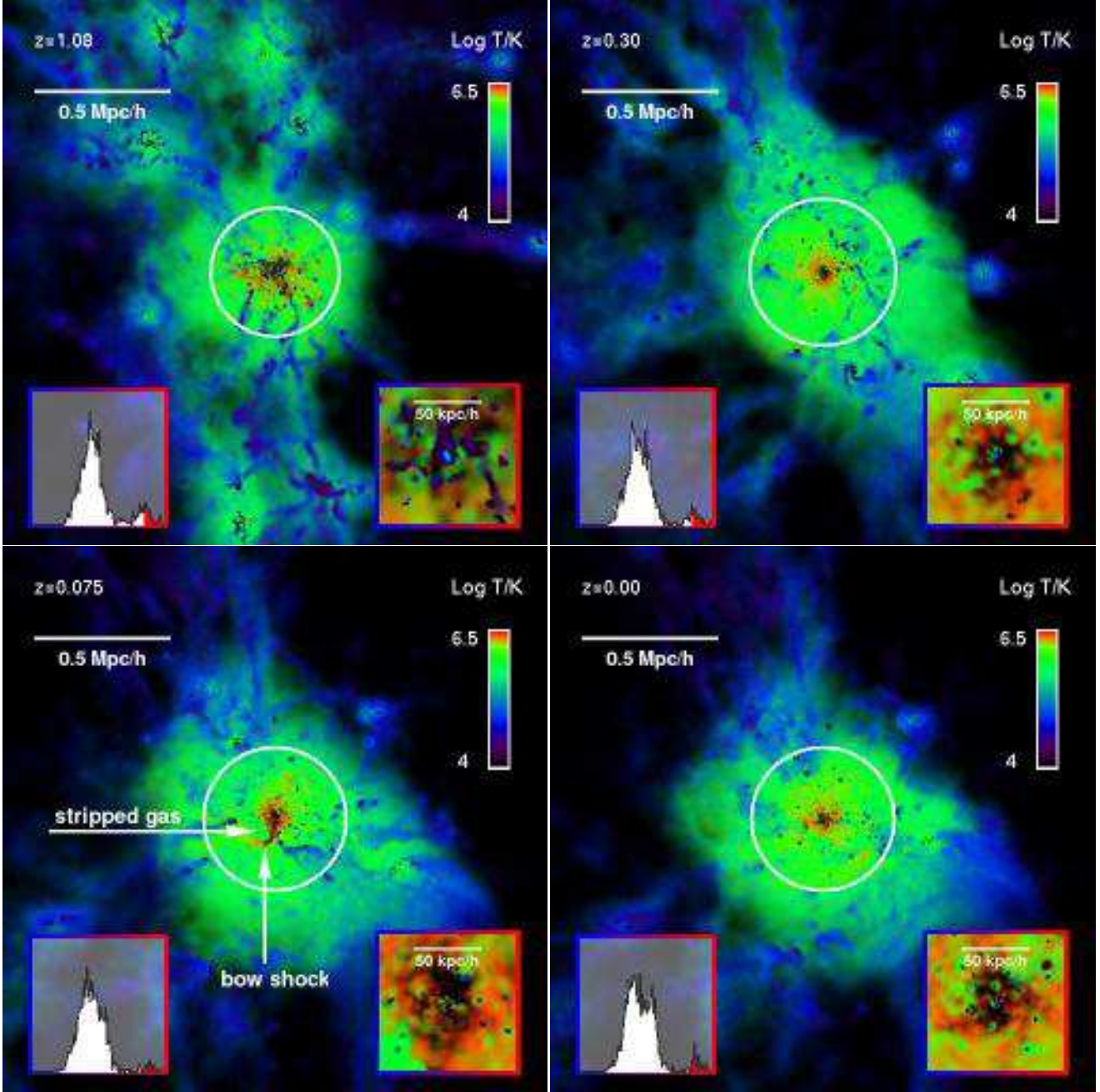


**Figure 4.** Continued. The presence of strong shock due to a satellite’s supersonic motion through the hot IGM and of a tail of ram-pressure stripped gas behind the shock is prominent at  $z \simeq 0.075$ .

of the gas it swallows. At  $M_{\text{bh}} \lesssim M_{\text{p}}^{\text{gas}}$ , it receives a ‘kick’ whenever it swallows a gas particle. This ‘kick’ could even throw it out of the galaxy. Our solution to this technical problem goes as follows. Initially, the black hole has been placed at the bottom of the gravitational potential and has been made to accrete at a very high rate. As several gas particles with momentum oriented at random are accreted at the same time, this ensures that the total momentum per unit mass accreted is small. We have used this procedure to grow a black hole that is essentially at rest with respect to the central part of its host galaxy. We have stopped the rapid growth when the black hole has reached a mass  $M_{\text{bh}} \gg M_{\text{p}}^{\text{gas}}$ . Since in our simulation  $M_{\text{p}}^{\text{gas}} = 1.48 \times 10^6 h^{-1} M_{\odot}$ ,

we have stopped the rapid growth of the seed black hole at  $M_{\text{bh}} = 2 \times 10^7 h^{-1} M_{\odot}$ . This value is  $\sim 10$  times larger than  $M_{\text{p}}$ , but clearly lower than the final black hole mass that we expect to find at  $z \sim 0$ . This prescription forms a seed black hole with  $M_{\text{bh}} = 2 \times 10^7 h^{-1} M_{\odot}$  already at  $z \simeq 5.4$ . At that redshift, the host galaxy may not be massive enough to host such a massive black hole, although there are claims that the black hole - bulge mass ratio was higher at high redshift (e.g. Walter et al. 2004; McLure et al. 2006; Peng et al. 2006). We have therefore subsequently frozen the growth of the black hole until the host galaxy has reached a stellar mass of  $M_{\star} \simeq 1.2 \times 10^{10} h^{-1} M_{\odot}$ . This happens as  $z \simeq 4.2$ .



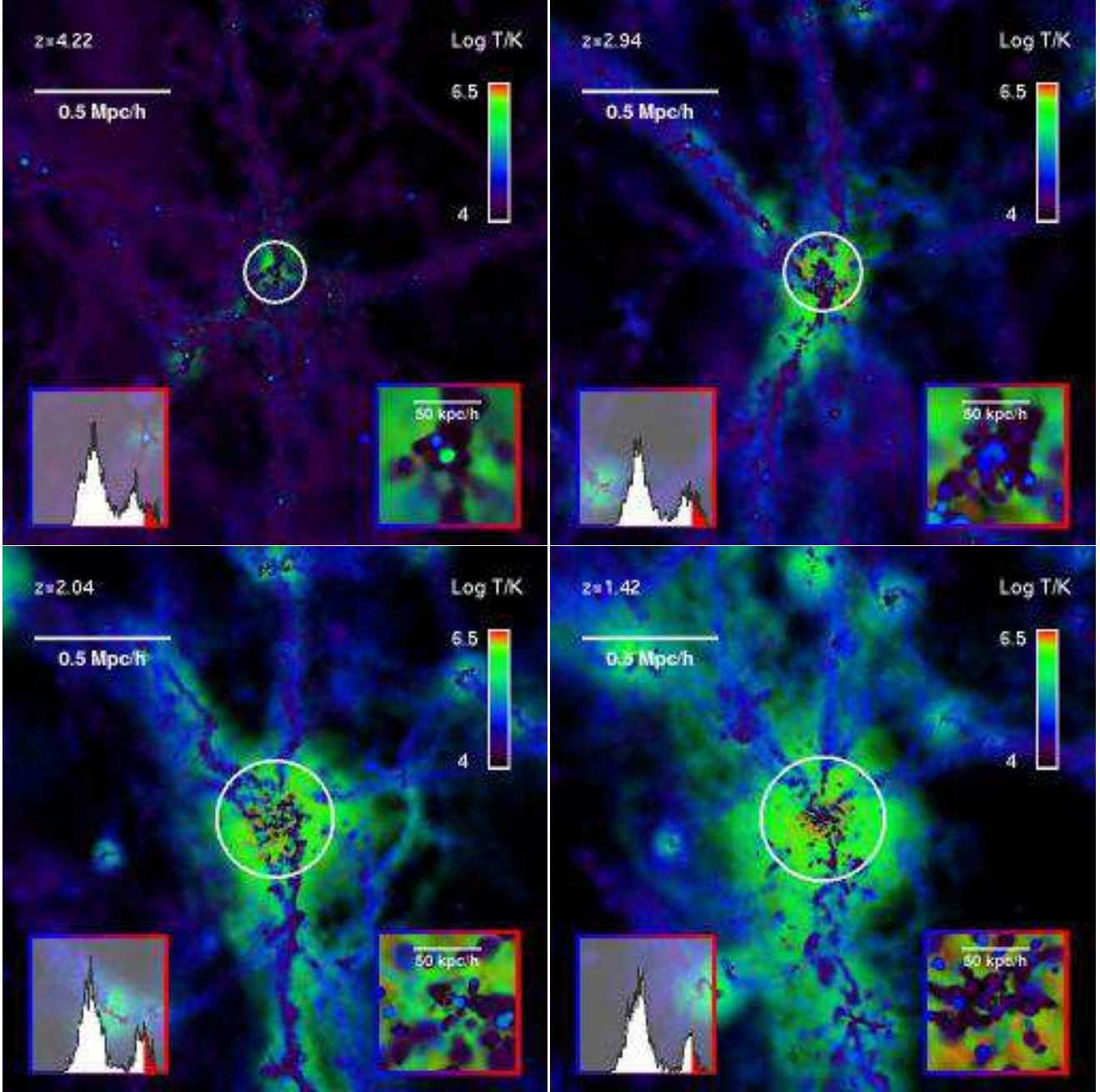


**Figure 5.** Density and temperature structure of the IGM in the simulation with AGN feedback (continues on the next page). Colour coding and histograms have the same meaning as in Fig. 4.

Following Springel et al. (2005a), the accretion rate of the black hole has been computed with the formula  $\dot{M}_{\text{bh}} = 4\pi\alpha(GM_{\text{bh}})^2\rho c_s^{-3}$  (Bondi 1952). The gas density  $\rho$  and the speed of sound  $c_s = \sqrt{p/\gamma\rho}$  have been evaluated on the SPH kernel of the black hole particle (the  $40 \pm 1$  nearest neighbours). The density of the interstellar medium smoothed on the scale of the computational resolution is much lower than the expected high densities around the black hole on the scale of the Bondi radius  $r_{\text{Bondi}} = GM_{\text{bh}}c_s^{-2}$ , where the Bondi formula applies. We have compensated for this by deliberately setting  $\alpha$  to the high value  $\alpha = 300$  instead of the value  $\alpha \sim 1$  (see also Hopkins et al. 2006). The choice of  $\alpha = 300$  is justified a

posteriori by observing that it produces a reasonable black hole mass at the end of the simulation. We have limited  $\dot{M}_{\text{bh}}$  by requiring that  $\epsilon\dot{M}_{\text{bh}}c^2$  cannot exceed the Eddington luminosity  $L_{\text{Edd}} \simeq 1.3 \times 10^{46} (M_{\text{bh}}/10^8 M_{\odot}) \text{ erg s}^{-1}$ .

Here we have assumed that the power released by the accretion of gas onto the black hole is  $\epsilon\dot{M}_{\text{bh}}c^2$  with a standard efficiency of  $\epsilon \sim 0.1$ , and that a fraction  $\beta = 0.05$  of this power is converted into heat and distributed to the same SPH kernel used for computing the accretion rate.

To implement numerically the actual accretion, we follow a similar stochastic approach as it is applied for regular star formation (Springel et al. 2005a). For this purpose, we compute for each gas particle  $j$  around a BH a probability:



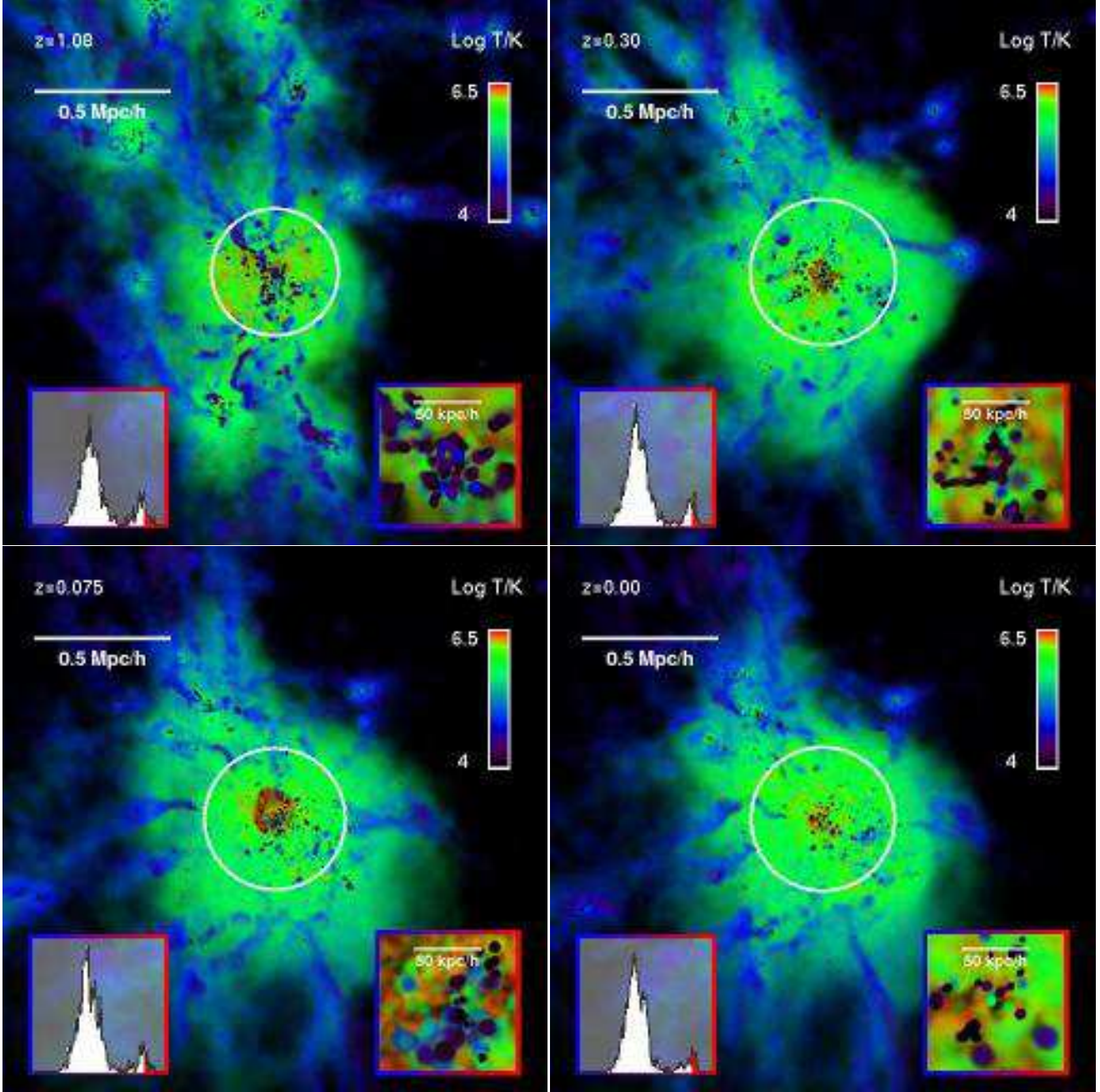
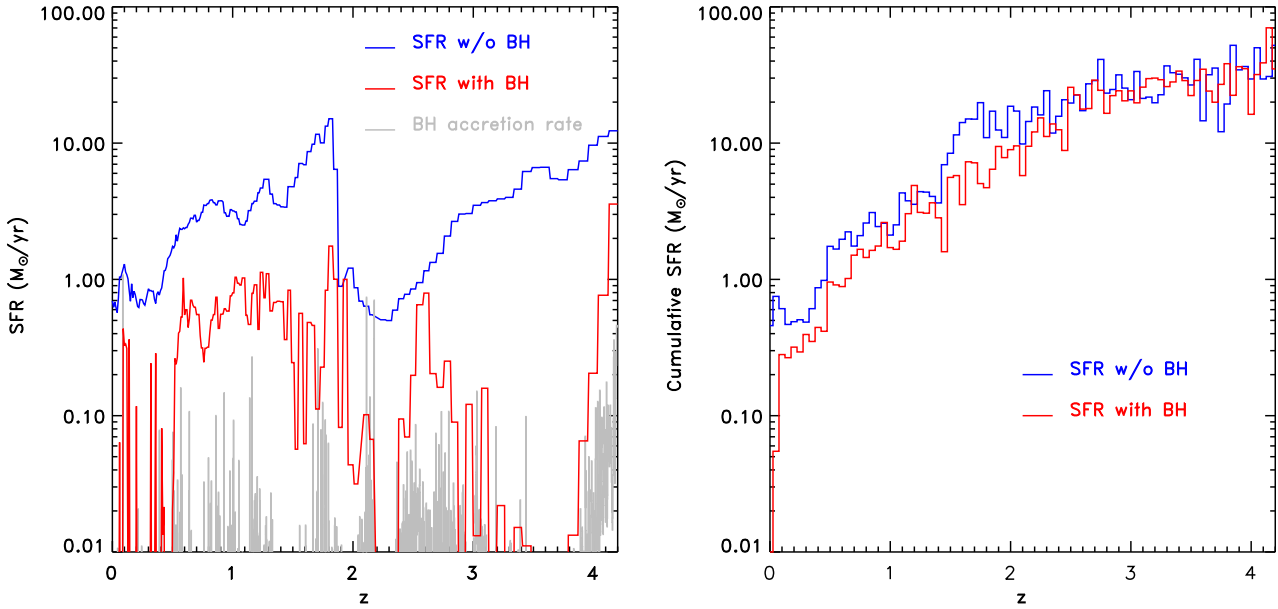


Figure 5. Continued.

$p_j = \frac{w_j \dot{M}_{\text{bh}} \Delta t}{\rho}$ , for being swallowed by the black hole. Here,  $\dot{M}_{\text{bh}}$  is the black hole accretion rate,  $\Delta t$  is the time-step,  $\rho$  is the gas density estimated at the position of the BH and  $w_j$  is the kernel weight of the gas particle relative to the BH. We then draw random numbers  $x_j$  uniformly distributed in the interval  $[0, 1]$  and compare them with the  $p_j$ . For  $x_j \leq p_j$ , the gas particle is absorbed by the BH, including its momentum. On average, this procedure ensures that the BH particle accretes the right amount of gas consistent with the estimated accretion rate  $\dot{M}_{\text{bh}}$ .

### 3 ANALYSIS METHODOLOGY

Two approaches are possible to extract galaxy masses, star formation rates, luminosities and colours from the simulation outputs. The first is to identify the particle that belong to the central galaxy by running a group-finding algorithm on the simulation outputs. The second is to convert the SPH outputs into virtual observations (.FITS files) by using a program that simulates astronomical images. The first approach is the one that is commonly used. It has the advantage that one has access to the full 6D phase-space information in the simulation outputs. The second approach has been developed by Contardo et al. (1998) and Cattaneo et al. (2005a). It has the advantage that luminosi-



**Figure 6.** Evolution of the star formation rate. The diagram to the left shows the instantaneous star formation rate within the radius containing 90% of the galaxy stellar mass at redshift  $z$ . The diagram to the right is based on all stars that end up within the 90% mass radius at  $z \sim 0$ . Therefore, it includes the stars formed in satellite galaxies that merge with central galaxy. The blue (red) lines refer to the simulation without (with) AGN feedback.

ties and colours are determined in a way that is consistent with standard observational procedures. The two approaches complement each other. We have used the first one to compute masses and star formation rates, the second one to investigate surface brightness profiles and isophotal shapes (Sersic indexes, ‘boxiness’ vs. ‘disciness’ and colour gradients), and both to compute magnitudes and colours. The results that we have found with the two methods are not quantitatively identical, but the differences are small and they do not affect any of the conclusions of this article. For instance, in the simulation without AGN feedback, the luminosity of the central galaxy estimated by the first method is  $M_V \simeq -21.0, -21.3, -21.8, -20.6$  at  $z \sim 0, 0.3, 1, 2$ , respectively. For comparison, the luminosities measured from the .FITS files at the same redshifts are  $M_V \simeq -21.1, -21.4, -21.8, -20.4$ , respectively. The differences between the results obtained with the two methods are not larger than photometric errors in real data. We now expand on the procedures used for these two approaches in greater detail.

### 3.1 Identifying galaxies in SPH simulations

To measure galaxy masses, we need a procedure to decide which stellar particles belong to a galaxy. For this purpose we have used an approximate friends-of-friends group finder that links all stellar particles within a linking length equal to the force resolution  $(2h^{-1} \text{ kpc})^2$  and have removed all

particles that are not gravitationally bound to the approximate friend-of-friend group to which they belong. (notice that for a linking length of  $2h^{-1} \text{ kpc}$  removing unbound particles makes little difference to the stellar mass).

We have used the Bruzual & Charlot (2003) stellar population synthesis model to compute the  $U$ ,  $B$  and  $V$  band magnitudes of the stars inside the galactocentric radius  $r_{90}$  containing 90% of the stellar mass  $M_{\text{star}}$  identified with the approximate friend-of-friend algorithm. We have made no attempt at modelling the extinction of stellar light by dust. Let  $\Delta M_{\text{star}}$  be the mass of the stars that have galactocentric distance  $< r_{90}$  and age  $< \Delta t = 10^7 \text{ yr}$ . We define the instantaneous star formation rate as  $\dot{M}_{\text{star}} \equiv \Delta M_{\text{star}} / \Delta t$ .

### 3.2 Observing the simulated Universe

The approach that we have just described has the advantage that it uses the full information available in the simulations. However, this procedure is quite different from the one that an observer would use. Therefore, the values that one infers may not be directly comparable to those that are measured in observational studies. For this reason, we have also devised an alternative procedure. After using the Bruzual & Charlot (2003) stellar population synthesis model to compute  $U$ ,  $B$  and  $V$  magnitudes for each stellar particle, we have used the software SkyMaker<sup>3</sup> (Bertin & Fouqué 2007) to simulate observations with the Hubble Space Telescope and convert the SPH outputs into .FITS files (see also Cattaneo et al. (2005b)), which has allowed us to perform our analysis by using standard software packages for astronomical data analysis.

<sup>2</sup> The approximate friend-of-friend group finder used for this work is publicly available at the URL <http://www-hpcc.astro.washington.edu/tools/tools.html>. This web site also contains a description of the algorithm.

<sup>3</sup> <http://terapix.iap.fr/soft>



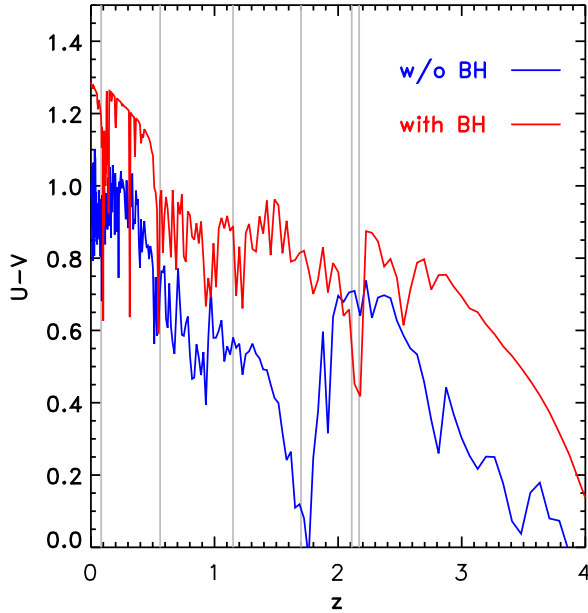


**Figure 7.** The  $U - V$  colours of the stellar population inside the radius containing 90% of stellar mass. The blue (red) line corresponds to the simulation without (with) AGN feedback. The vertical grey lines mark the redshifts at which the AGN shines with  $M_B \lesssim -21$ . The colours shown here were computed with the procedure described in Section 3.1. Some strong blue colour peaks are due to close star-forming companions, which could not be disentangled from the central galaxy.

The analysis of the virtual data has been performed on .FITS files that cover a field of  $200 \times 200 h^{-2} \text{kpc}^2$ . The field of view is centred on the central galaxy. After masking small or distant satellites, we have used GALFIT (Peng et al. 2002) to fit the surface brightness distribution of the central galaxy and its neighbours with a Sersic profile  $\Sigma = \Sigma_e \exp\{-b_n[(r/r_e)^{1/n} - 1]\}$ , where  $b_n$  is set by the condition that half of the light is contained in the half light radius  $r_e$ . By this procedure we have determined the galaxy’s magnitude, half light radius and Sersic index  $n$  for each of the three bands for which synthetic images have been generated.

GALFIT has also allowed us to determine the isophotal shape of our synthetic galaxies. Deviations from purely elliptical isophotes are quantified by fitting isophotes with the functional form

$$r = \left( |x - x_c|^{c+2} + \left| \frac{y - y_c}{q} \right|^{c+2} \right)^{\frac{1}{c+2}}. \quad (1)$$

Here  $(x_c, y_c)$  define the centre of the ellipses,  $r$  the semi-major axis and  $q$  the axis ratio. For  $c = 0$ , Eq. 1 reduces to that of an ellipse. The cases of disk and boxy ellipticals correspond to  $c < 0$  and  $c > 0$ , respectively.

As our purpose is to concentrate on galaxy evolution, even in the simulation with AGN feedback we have assumed that the AGN is obscured (type 2) at all times, so that the host galaxy photometry is not contaminated by AGN light. Therefore, we have avoided the additional uncertainties related to the removal of bright nuclear point sources, which is needed when studying the host galaxies of type 1 AGNs.

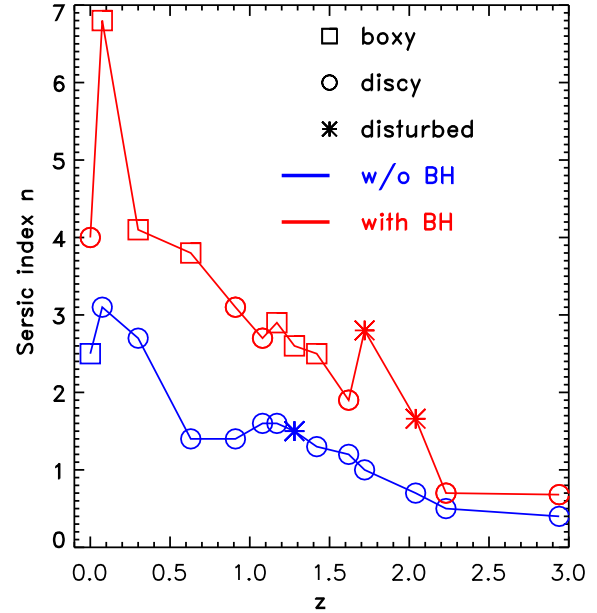


**Figure 8.** Best fit single Sersic index for the major timesteps shown in Fig. 2 and 3. The red and blue curves refer to the simulations with and without AGN feedback, respectively. Galaxies have been classified into discy (round symbols) and boxy (square symbol) according to the value of the  $c$  GALFIT parameter (Section 3.2). Results for clearly disturbed systems have been marked with asterisk and should be taken with caution. The result of the simulation with AGN feedback at  $z = 0$  should also be taken with caution because we can still see an underlying disc remnant from the last major merger.

#### 4 RESULTS WITHOUT AGN FEEDBACK

We start by analysing the results of the simulation without black hole. The results of the simulation with AGN feedback are shown for comparison but they will be discussed in the next section.

The evolution of the luminous component is driven by the hierarchical growth of the dark matter halo through smooth accretion and merging. The dark matter halo grows from  $M_{\text{halo}} \sim 10^{11} h^{-1} M_{\odot}$  at  $z \sim 5$  to  $M_{\text{halo}} \sim 3 \times 10^{12} h^{-1} M_{\odot}$  at  $z \sim 0$  (Fig. 1). Two major mergers with other haloes are recognisable, the first at  $z \sim 2.7 - 2.9$ , the second at  $z \sim 0.7 - 0.9$ . Qualitatively, the growth of the central galaxy follows that of the dark matter halo. E.g., the halo merger at  $z \sim 2.7 - 2.9$  is followed by a major merger between galaxies at  $z \sim 2$ . This merger is clearly visible in Fig. 1 and Fig. 2.

Fig. 2 and Fig. 3 summarise the key moments in the evolution of the central galaxy from  $z \simeq 4.2$  to  $z \simeq 0$  in the cases without and with AGN feedback, respectively.

Our simulations support the notion that the formation of galaxies at the centres of dark matter haloes is due to accretion of cold filamentary flows (Kereš et al. 2005; Dekel & Birnboim 2006). At  $z = 4.22$ , the accretion of cold streams onto the central galaxy is clearly visible in the enlargements of the central region (Figs 4 and 5). In our simulations, the accretion of cold flows form galaxies with disc-

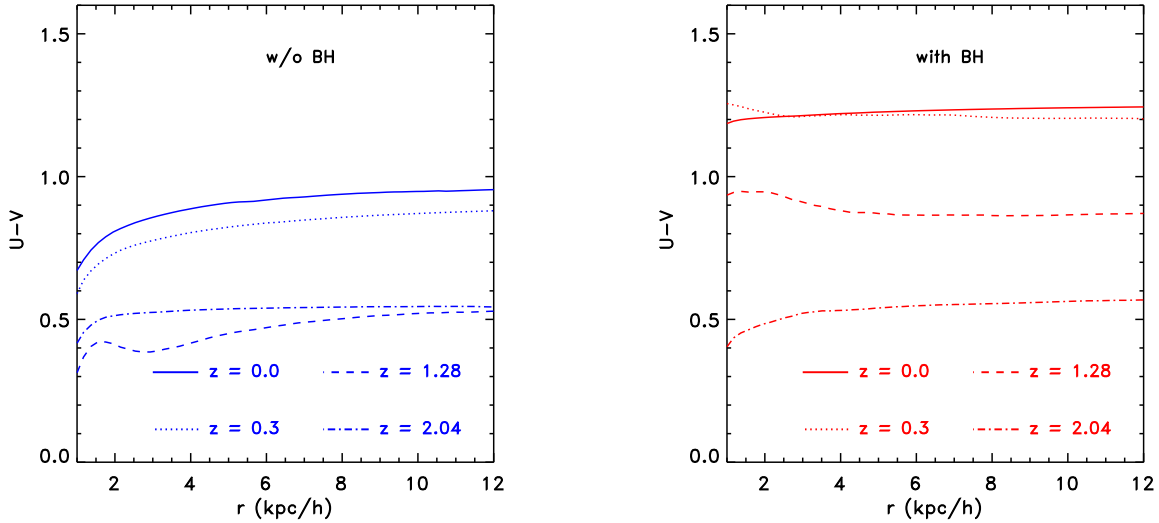


**Figure 9.**  $U - V$  galaxy colour profiles in the simulations without (left panel) and with (right panel) AGN feedback for certain key moments in their evolution. The profiles without AGN always show the same behaviour with a clear drop toward the centre. In the case with AGN feedback, we clearly see standard colour gradients (the colour becomes redder moving inward) after a period of passive evolution and reversed colour gradients when star formation is reactivated by mergers.

like morphologies. An edge-on disc is clearly recognisable in Fig. 2 at  $z \simeq 2.23 - 4.22$ .

The galaxy mass grows proportionally to the halo mass until  $z \simeq 4.3$ . At this redshift, the stellar mass of the central galaxy is  $M_{\text{star}} \sim 0.7 f_b M_{\text{halo}}$ , where  $f_b \simeq 0.15$  is the cosmic baryonic fraction (Fig. 1). The situation changes at  $z \lesssim 4$ . Due to the higher halo mass, a large fraction of the gas that flows into the virial radius is heated by shocks before it can reach the central galaxy. Fig. 4 makes this point very clearly. From  $z \simeq 2.94$ , the  $\sim 10^6$  K hot spherical halo (in green) fills an increasingly large fraction of the volume inside the virial radius (white circle). The cold gas that manages to stream deep into the halo fragments into clumps before it can be accreted onto the central galaxy (see the enlargements of the central region). Therefore, already at  $z \sim 4$ , the supply of cold gas to the central galaxy has started to dry out. This is the reason why the growth of the galaxy stellar mass between  $z \sim 4$  and  $z \sim 2$  is very limited (Fig. 1). As soon as the galaxy stops to accrete gas, the star formation rate begins to decrease (Fig. 6) and the colour starts to become redder (Fig. 7). This can also be appreciated by comparing the colours at  $z \simeq 4.22$  and  $z \simeq 2.23$  in Fig. 2. Without refuelling by galaxy mergers, the galaxy is already on its way to becoming an early-type spiral.

However, while the star formation rate in the central galaxy is already steeply declining soon after  $z \sim 4$ , the total star formation rate within the halo is only exhibiting the same steep decline after  $z \sim 2$ . Fig. 6 shows this point by comparing the central galaxy’s star formation rate (left) with the cumulative star formation rate of the central galaxy and the satellite galaxies that will merge with the central galaxy before the end of the simulation at  $z \sim 0$  (right). The different behaviour in the two panels of Fig. 6 is due to the collapse of gas in substructures along the filaments. They contribute to the growth of the central galaxy in two ways: directly, by depositing gas onto it, and indirectly, by

forming satellites, which then fall into the central galaxy. The second mode becomes the predominant mode of galaxy growth after the formation of a hot halo. Comparing the two panels in Fig. 6 shows that that the second mode contributes to a substantial fraction of the final galaxy mass.

Another process that becomes important and affects the evolution of satellite galaxies after the formation of a halo of hot gas is ram pressure stripping. The effects of ram pressure stripping are clearly recognisable at  $z \simeq 0.075$  and  $z \simeq 0$  in Fig. 4. The green ‘tongues’ to the left of the hot central region are trail of gas stripped from galaxies that have entered the virial radius and moved through the hot gas. In front of these ‘tongues’ strong shocks (red) due the galaxies’ supersonic motions are clearly visible.

The quiescent merging history at high redshift is the reason why the galaxy has been able to maintain a spiral morphology until  $z \simeq 1.96$ . The interaction at  $z \simeq 3.56$  leads to the accretion of tidally disrupted material. It causes a temporary increase in the star formation rate (Fig. 6) but it has no effect on the galaxy mass. By  $z \simeq 2.04$ , the galaxy has become part of small group. An approximately equal mass merger with another disc galaxy at  $z \simeq 1.72$  transforms our spiral galaxy into an object whose visual morphology is more consistent with an elliptical galaxy (Fig. 1 and Fig. 2). However, a quantitative analysis of its photometry shows that its Sersic index is more consistent with a spiral galaxy both before ( $n \simeq 0.7$ ) and after ( $n \simeq 1.3$ ) the merger. This merger is followed by another major merger, with a 1 : 2 mass ratio, at  $z \simeq 1.28$ . The latter occurs after two satellite galaxies have first merged into one. After this second merger, the Sersic index rises to  $n \simeq 1.6$ , but is still outside the range that we expect for an elliptical galaxy. These two major mergers are clearly visible as star formation rate peaks in Fig. 6. The peak at  $z \sim 0.8$  is due to the accretion of gas stripped from tidally disrupted companions. Only after the star formation rate starts to decline ( $z \lesssim 0.6$ ) does the Sersic index reaches



values more typical of an elliptical galaxy (e.g.  $n \simeq 2.7$  at  $z \sim 0.3$ ). The accretion of tidal features, one of which is also visible in Fig. 6 at  $z \simeq 0.075$ , temporarily reactivates star formation by bringing fresh gas into the galaxy. This effect is clearly visible as a central light excess in an otherwise red elliptical galaxy (Fig. 2). This picture is also supported by the colour gradients in Fig. 9, where we see a steep drop of the  $U - V$  colour toward the galactic centre. Consequently, the galaxy colour is not as red as it is expected for a red sequence galaxy (Fig. 7 and 10). This finding is consistent with previous studies by Meza et al. (2003) and Naab et al. (2007), who also reported values of  $U - B$  that were not increasing toward the centre. Elliptical galaxies with blue central regions are observed (E+A galaxies), but they are not typical of the elliptical population. While an individual object cannot be used to draw statistical conclusions, the simulations carried out until now support the conclusion that a mechanism that removes the cold gas accumulated in galaxy mergers is necessary to form truly red elliptical galaxies. Elliptical galaxies formed in simulations that do not contain such a mechanism have colours in the ‘green valley’ that separates the blue and the red population on the colour – magnitude diagram (Fig. 10).

## 5 THE SIMULATION WITH AGN FEEDBACK

### 5.1 Dynamical evolution

The dynamical evolution in the simulation with AGN feedback is very similar to that in the simulation without black hole until AGN feedback is activated at  $z \simeq 4.2$ . Small differences in the dynamics before  $z \simeq 4.2$  are due not only to the fact that a small mass of gas has been used to form a supermassive black hole (Section 2) but also to differences in the timesteps of the two simulations. On large scales, the dark matter distribution is very similar with and without AGN feedback even after  $z \simeq 4.2$ . Inside the virial radius, we continue observe a similar mass distribution of dark matter substructures, but substructures are not found at the same positions because even small differences become very large in a few dynamical times (the evolution is highly non-linear and phase mixing occurs).

The reason why we have not turned AGN feedback on from the beginning is computational rather than physical (Section 2). At  $z \sim 4.2$ , the galaxy stellar mass is  $M_* \simeq 10^{10} h^{-1} M_\odot$  and the black hole mass is  $M_{\text{bh}} \simeq 2 \times 10^7 h^{-1} M_\odot$ . The presence of a large mass of cold gas that has accumulated unhindered inside the central galaxy means that the accretion rate at  $z \simeq 4.2$  is very large. The black hole swallows  $5 \times 10^6 h^{-1} M_\odot$  of gas in a very short span of time (Fig. 11). The energy injection that accompanies the fast growth of the black hole at  $z \sim 3.9 - 4.2$  causes an explosion, which reheats or blows away nearly all the cold gas that is present in the galaxy at that time. Star formation is quenched until  $z \sim 3$ . The timing and the intensity of this accretion episode are artificial as they depend on the arbitrary choice of the redshift at which AGN feedback is activated. However, it is energy and not power that matters when we are concerned with the effects on cosmological timescales as opposed to the effects on the timescale of the active phase,  $\sim 10^7 - 10^8$  yr. The total mass of  $\sim 3 \times 10^7 M_\odot$

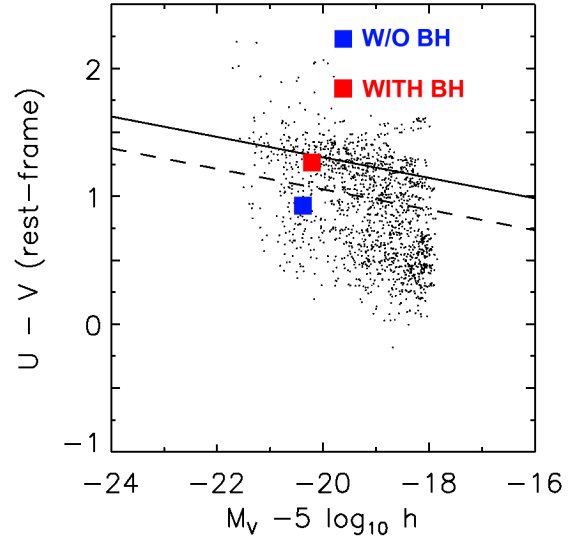


**Figure 10.** The  $U - V$  colour and the  $V$ -band magnitude of the central galaxy at  $z \simeq 0$  in the simulation without (blue symbol) and the simulation with (red symbol) AGN feedback. The results of the simulations have been superimposed on a synthesised  $U - V$  vs.  $M_V$  colour – magnitude diagram for a volume-weighted sample of  $14.5 \leq r \leq 16.5$  Sloan Digital Sky Survey galaxies, which we have reproduced from Bell et al. (2004).

that our black hole has accreted by  $z \sim 2.6 - 3$  (Fig. 11) and thus the total energy that it has deposited into the IGM by that redshift are not unreasonable. We also note that the stellar mass (Fig. 1) and the star formation rate (Fig. 6) at  $z \sim 2.6$  are similar in the simulations with and without AGN feedback. Therefore, we conclude that, although the evolution at  $3 \lesssim z \lesssim 4$  is affected by the arbitrary way with which we have switched on AGN feedback, the memory of the explosive growth at  $z \simeq 4.2$  is lost by  $z \sim 2.6 - 3$  (Fig. 6). For this reason, we concentrate on the evolution after  $z \lesssim 3$ .

The reactivation of star formation at  $z \sim 3$  is due to a gas-rich minor merger (Fig. 3:  $z \simeq 2.94$ ). Despite the impression of an elliptical morphology, the remnant at  $z \simeq 2.23$  is fitted by a Sersic profile with  $n \simeq 0.7$ . This merger is followed by two major mergers at  $z \simeq 2.04$  and  $z \simeq 1.72$  (Fig. 3). The first of the two is a nearly equal mass merger. Their combined mass growth is similar to the one produced by the single major merger observed at  $z \sim 1.72$  in the simulations without AGN feedback. It is interesting to see how the different kinematics of the mergers at  $z \simeq 2.04$  and  $z \sim 1.72$  affect black hole growth and star formation. The first merger is nearly head-on. Therefore, most of the gas in the companion is brought straight into the centre. The result is a flare of AGN activity with  $M_B \sim -22.6$ , where the black hole reaches the Eddington limit. We also observe a period of enhanced star formation clearly visible as a peak in  $U - V$  colour in Fig. 7. In the second merger, the two galaxies merge with a spiral motion (Fig. 3). Their tidal interaction induces a burst of star formation before their cores have time to merge. It is at that point that the growth of the black hole is reactivated and quenches star formation (Fig. 6). In this second case, the peak star formation rate is

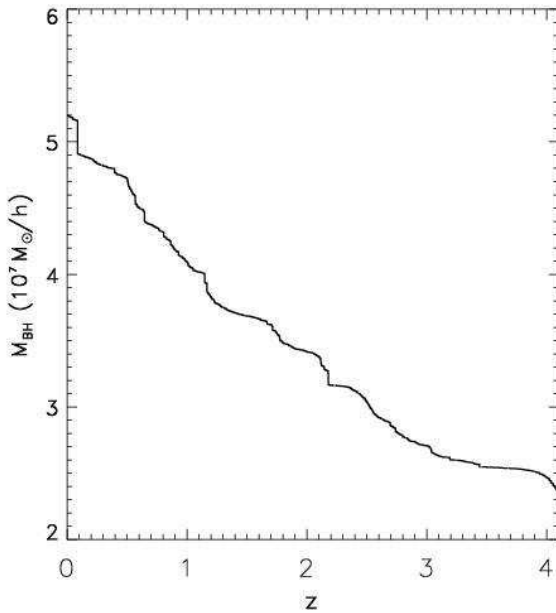


**Figure 11.** The growth of the black hole in the simulation with AGN feedback. Besides the initial growth, four main growth episodes are identifiable. They coincide with the major merger at  $z \sim 2.2$ , the borderline merger at  $z \sim 1.1$ , the accretion of a tidal feature at  $z \sim 0.6$  and the major merger at  $z \sim 0.1$ . Only the first and the last correspond to accretion rates approaching the Eddington limit (see Fig. 6 and the caption to Fig. 3). Notice that this diagram uses a linear rather than logarithmic mass scale.

higher but the peak AGN luminosity is lower ( $M_B \sim -21.7$ ) because the AGN only switches on in the final stage of the merger, when there is little gas left. After the  $z \simeq 1.72$  merger, at  $z \simeq 1.42$ , the galaxy has the appearance of a red-dish mildly boxy elliptical galaxy with Sersic index  $n \simeq 2.5$ . The ‘noisy’ star formation rate history at  $z \sim 0.6 - 1.3$  is the result of a minor merger at  $z \sim 1.08 - 1.18$ , which activates an AGN with  $M_B \sim -21.7$ , and of the accretion of tidally disrupted clouds from a number of close small companions. The gas brought in by these events is the reason why the isophotes return to be temporarily discy. The accretion of a tail of tidal debris (the blue half ring in Fig. 3) triggers an AGN with  $M_B \sim -21$  at  $z \simeq 0.63$ . Star formation is, therefore, first reactivated, and then quenched. From this point onwards, the specific star formation rate is the same range as the values inferred for red sequence galaxies in the Sloan Digital Sky Survey (Kauffmann et al. 2004).

By  $z \sim 0.1$ , when a new merger is about to occur, the galaxy has evolved into a boxy elliptical with Sersic index  $n \simeq 6.8$ . The increase in the value of the Sersic index and the transition from discy to boxy isophotes occur gradually and do not appear as immediate results of galaxy merging, suggesting that interactions with small companions and internal dynamical evolution have played a role in this transformation. However, another important element is the fading of discs of young stars formed by dissipational infall in galaxy mergers. These discs contribute to a small fraction of the mass of an elliptical galaxy but to a less small fraction of its light. They therefore contribute to the discy morphology of the remnants of dissipational mergers. However,

when the newly formed stars age, their luminosity contrast with respect to the preexisting stellar population weakens. Therefore, the galaxy evolves into an elliptical with boxy isophotes. We have verified this interpretation by considering the central galaxy at  $z \simeq 0.91$  and aging it passively to  $z \simeq 0$  without changing anything of its mass distribution and kinematics. The galaxy passed from being a discy elliptical with  $n \sim 3.1$  to being a boxy elliptical with  $n \sim 4.3$ , although passive fading alone does not bring the Sersic index up to  $n \gtrsim 6$ .

A final major merger with a disc galaxy at  $z \simeq 0.075$  is not able to reactivate star formation effectively because its gas content is immediately blown away by a powerful AGN outbursts with  $M_B \sim -23$ . Late mergers are less effective at bringing gas into the centre not only because gas is consumed by star formation but also due to ram pressure stripping of the ISM by the hot gas (Section 4). The  $z \simeq 0$  remnant of this final merger has a Sersic index of  $n \simeq 4.0$  and slightly discy isophotes related to the presence of an underlying disc from the last major merger. Due to quenching of star formation by AGN feedback, the galaxy is now clearly on the red sequence of the colour – magnitude diagram (Fig. 10).

## 6 THE ENTROPY OF THE INTERGALACTIC MEDIUM

In our simulation, the primary effect of AGN feedback is to quench star formation by expelling the galaxy’s ISM. However, the development of a cooling flow could reactivate star formation and move elliptical galaxies back to the blue cloud. To address the ‘maintenance’ problem in the context of our simulations, we first need to determine the cooling time of the hot gas.

For this purpose, it is useful to introduce the entropy constant  $S \equiv kTn^{-2/3}$  because it allows to write the cooling time as the product of two terms (Scannapieco & Oh 2004):

$$t_{\text{cool}} = \frac{\frac{3}{2}nkT}{n_e^2\Lambda(T, Z)} = \left( \frac{S}{10 \text{ keV cm}^2} \right)^{\frac{3}{2}} \times \frac{3}{2} \left( \frac{\mu_e}{\mu} \right)^2 \frac{1}{(kT)^{\frac{1}{2}}\Lambda(T, Z)} (10 \text{ keV cm}^2)^{\frac{3}{2}}. \quad (2)$$

The first term is a measure of the entropy and, therefore, it does not change when the gas is compressed or expands adiabatically. The second term depends on the temperature and the metallicity only. For a fully ionised gas,  $\mu \simeq 0.59$  and  $\mu_e \simeq 1.1$ . In the range of temperatures that we encounter in our simulations ( $T < 10^8$  K), the factor on the second line of Eq. (1) has an absolute minimum. Its value is  $\sim 2$  Gyr for the primordial cooling function used in our simulations, and  $\sim 200$  Myr for  $Z = 0.3Z_\odot$ . Therefore, the entropy constant  $S$  determines the minimum cooling time for a given metallicity. We use the notion of minimum cooling time to interpret the evolution of the IGM entropy distribution, where by IGM we mean the gas below the density threshold for star formation, which separates the IGM from the ISM.

The IGM entropy distribution is strongly bimodal both without and with AGN feedback (Fig. 12). The low entropy peak corresponds to the cold gas in the filaments. The high entropy peak corresponds to dilute hot gas at



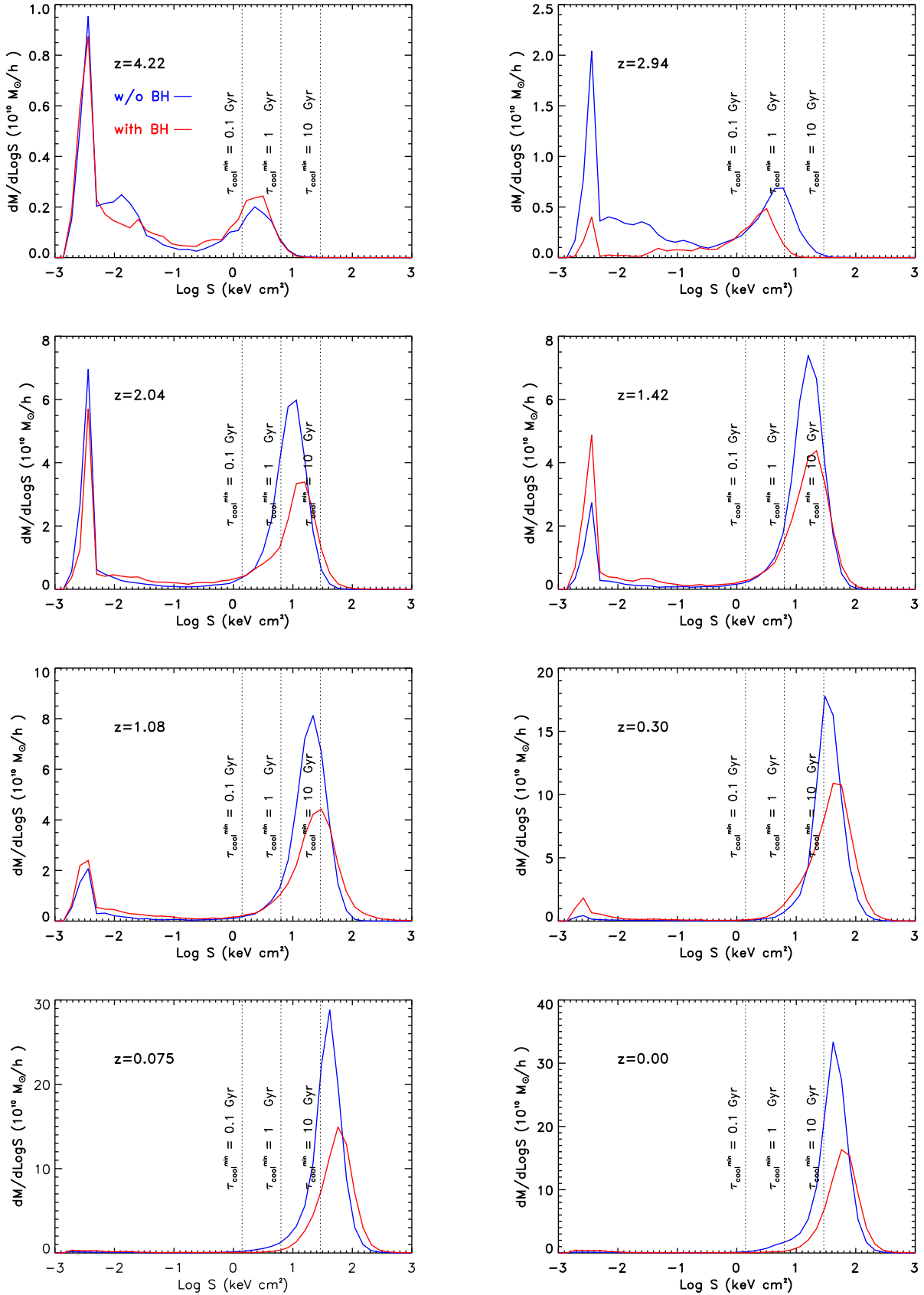


**Figure 12.** Entropy distribution of the IGM inside the virial radius in the simulation without (blue) and the simulation with (red) AGN feedback. The ISM (the gas with  $\rho > \rho_{\text{th}}$ , where  $\rho_{\text{th}}$  is density threshold for star formation) has not been shown on these diagrams. The vertical dotted lines mark the values of the entropy constant  $S$  that correspond to a minimum cooling time of 0.1 Gyr, 1 Gyr and 10 Gyr for primordial metal abundances.

the virial temperature ( $T_{\text{vir}} \sim 2 - 3 \times 10^6 \text{ K}$  at  $z \sim 0$ ) and it is where we expect it from the simple calculation  $S = kT_{\text{vir}}(\Omega_b \rho_{\text{vir}}/\mu m_p)^{-2/3} \propto M_{\text{vir}}^{2/3} \rho_{\text{vir}}^{-1/3}$ . Gas that flows into the virial radius at lower  $z$  is shocked to higher entropy because its density is lower and the potential well of the dark matter is deeper. If we compare Fig. 12 with the density histograms in Figs. 4–5, the gas in the low entropy peak corresponds the dense (cold) IGM, while the gas in the high entropy peak corresponds to the low density phase of the IGM. The ISM (the red area under the density histograms in Figs. 4–5) is not considered in Fig. 12.

As we move from high to low redshift, the cold IGM progressively disappears. It contains a small fraction of the mass at  $z \sim 0.3 - 1$ . By  $z \sim 0.1$  it has almost completely vanished. Most of the gas is in the hot IGM, and the cold gas that remains is in the ISM (Figs. 4–5). In addition, more and more baryons pass the entropy threshold above which their cooling time is longer than the age of the Universe. At  $z \simeq 0.3$  most of the IGM has  $t_{\text{cool}} \gtrsim 10 \text{ Gyr}$ .

Fig. 12 shows that AGN feedback does not make a huge difference. We now explain how we can understand this result by considering the total energy output of supernova and AGN feedback integrated over the lifetime of the Universe. Our model of supernova feedback assumes that supernovae return 10% of the mass that makes stars to the ISM. This mass is returned with a temperature of  $T_{\text{SN}} = 10^8 \text{ K}$ . The energy efficiency of supernova heating is, therefore,  $\epsilon_{\text{SN}}^{\text{heat}} = \frac{1}{2} k T_{\text{SN}} (0.1 M_{\odot} / \mu m_p) / (M_{\odot} c^2) \sim 2 \times 10^{-6}$ . The energy efficiency of AGN heating is much higher ( $\epsilon_{\text{BH}}^{\text{heat}} = \beta \epsilon \sim 5 \times 10^{-3}$ ) but its effectiveness is suppressed by a factor equal to the black hole-to-stellar mass ratio at  $z = 0$ ,  $M_{\text{bh}}/M_{\text{star}} \sim 5 \times 10^{-4}$ . When we multiply  $\beta \epsilon$  by this factor, we find an effective efficiency of  $2.5 \times 10^{-6}$ . Therefore, in our simulation, black hole and supernova heating are comparable. This is partly because our black hole is not very massive. Its mass at  $z = 0$  is only  $M_{\text{bh}} \simeq 5.2 \times 10^7 h^{-1} M_{\odot}$ . Typical black hole masses in elliptical galaxies with  $M_{\text{star}} \sim 10^{11} h^{-1} M_{\odot}$  are  $\sim 3 - 4$  times larger. However, there is also a compensation mechanism. Without AGN heating, there is more star formation and, therefore, more supernova heating. However, strong supernova feedback is only possible in blue (star-forming) galaxies. Therefore, the feedback from type II supernovae included in our simulations cannot be used to prevent the reactivation of star formation in elliptical galaxies (see Ciotti & Ostriker 2007 for a discussion of the role of type I supernovae in this context).

A closer look at the red and the blue curves in Fig. 12 shows two important differences. First, at  $z \simeq 0.075$  and  $z \sim 0$ , there is a small but clearly visible tail with  $\tau_{\text{cool}}^{\text{min}} < 1 \text{ Gyr}$  under the blue curve. There is no such tail under the red curve, which is slightly shifted and skewed towards higher value of  $S$ . In other words, the mean entropy may be similar, but the chances that some hot gas will manage to cool in the next billion years are much smaller in the simulation with AGN feedback. Second, the total mass under the red curve is lower than the total mass under the blue curve. This is due to the fact that a quarter of the baryons in the hot IGM have escaped the virial radius in the case of the simulation with AGN feedback.

In our simulations the reactivation of star formation and black hole accretion is mostly due to mergers. Cooling flows onto the central galaxy do not play a major role

in replenishing the central galaxy with cold gas. Work by Naab et al. (2007) suggests that this would remain true even if both AGN and supernova feedback were turned off. However, this occurs because both Naab et al. (2007) and we have computed cooling for primordial metal abundances. For  $Z = 0.3 Z_{\odot}$ , the minimum cooling time is over ten times shorter. In fact, there is evidence that feedback from slowly accreting radio sources plays an important role in solving the cooling flow problem (Fabian et al. 2002, 2003; Forman et al. 2005; Voit & Donahue 2005; Best et al. 2006; Dunn & Fabian 2006; Fabian et al. 2006; Rafferty et al. 2006), even if these observations are primarily concerned with galaxy clusters rather than with smaller systems, such as the one that we have simulated.

## 7 METAL ENRICHMENT

AGN winds contribute to the metal enrichment of the IGM by lifting highly enriched gas from the galactic centre. Their potential importance is demonstrated by the diagram in Fig. 13, which shows the mean IGM metallicity as a function of its overdensity with respect to the mean baryonic density of the Universe. Without AGN feedback, metals are confined to the vicinities of the galaxies in which they are produced (blue curve). In contrast, AGN feedback leads to a strong increase of the global metallicity of the IGM, which is easily overpredicted already at  $z \sim 3$  (red curve).

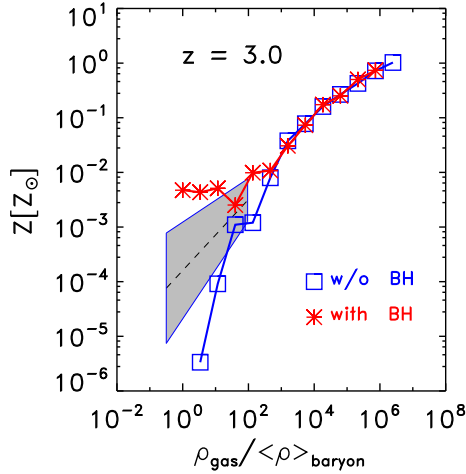
The model of the ISM that we have used for this work does not allow the effective generation of supernova winds because it is based on the assumption that the cold and the hot phase are in pressure equilibrium. Springel & Hernquist (2003) have developed a modified version that does it. They have demonstrated that supernova driven winds can also be important for the metal enrichment of the IGM, although they are not sufficient to account for it quantitatively.

Fig. 13 shows that the AGN feedback model and the efficiency assumed in this study over-enrich the IGM. However, what this work demonstrates is that even moderate AGN winds could play an important role in the chemical evolution of the IGM at high redshift.

## 8 DISCUSSION AND CONCLUSION

We have used cosmological hydrodynamic simulations with the SPH code GADGET-2 to study the formation of the central galaxy in a halo with a final mass of  $M_{\text{halo}} \simeq 3 \times 10^{12} h^{-1} M_{\odot}$  at  $z = 0$ . The simulations include several baryonic processes, e.g. the presence of a photoionising UV background, radiative cooling, the formation of a two-phase ISM, star formation, supernova feedback, the evaporation of cold clouds and the chemical enrichment of the ISM. The model used to describe these processes is that by Springel & Hernquist (2003). We have also run simulations where we include the growth of a central black hole (computed with the Bondi 1952 model) and its effects on the ISM/IGM (5% of the power released by black hole accretion is instantaneously thermalised in the surrounding gas). This model for black hole accretion and feedback was developed by Springel et al. (2005c) and has been used in several publications (e.g. Springel et al. 2005b; Hopkins et al. 2005;





**Figure 13.** Mean gas metallicity at  $z \sim 3$  as a function of its overdensity with respect to the mean baryonic density of the Universe. The blue and red curves correspond to the simulations respectively without and with AGN feedback. The grey shaded area shows Schaye et al. (2003)’s determination of the metallicity of the IGM at  $z \sim 3$  as traced by CIV. Although the data themselves are considerably uncertain, we clearly see that the model without AGN feedback seriously underestimates the metallicity of the IGM at baryonic overdensities  $\lesssim 10$ , while the model with AGN feedback overestimates it.

Cuadra et al. 2006; Li et al. 2007). The main difference between this work and previous studies is not in the physics, but rather in the system that we have chosen to simulate (the central galaxy of a group instead of an isolated merger or a cluster) and in the questions that we have addressed. This paper is focussed on the the interplay between gas accretion and merging in the development of galactic morphologies, and on the role of AGN feedback in the origin of the colour – morphology relation. It is also the first work of this kind to discuss the effect of AGN feedback on the photometry of early type galaxies, the redshift evolution in the properties of quasar hosts, and the impact of AGN winds on the chemical enrichment of the intergalactic medium (IGM).

Our work supports the notion that the early phases of the formation of galaxies are driven by the accretion of cold filamentary flows. Our simulations show that this mode of galaxy formation only forms discs. Elliptical morphologies only appear after galaxy mergers have occurred. There is a clear parallel between the growth of the dark matter halo and the growth of the central galaxy via merging (Fig. 1). These results were largely expected but they are important because they provide a powerful confirmation of the same assumptions that are used in semianalytic models of galaxy formation (e.g. Bower et al. 2006; Cattaneo et al. 2006; Croton et al. 2006).

Disc star formation rates at  $z \sim 4$  are about as high as the peak star formation rates in major mergers at later redshifts (in our simulations mergers start being important at  $z \sim 2$ ). That is because the merging galaxies have a gas-to-stellar mass ratio of  $\sim 0.1$  by the time the first major merger occurs. However, already at  $z \sim 4$  the filaments start to dry out, they fragment and they are no longer connected to the disc of the central galaxy. Therefore, the cen-

tral galaxy’s star formation rate begins to decline as it is progressively running out of gas. At the point where the cooling time overtakes the heating time, the two are of the order of  $\sim 1$  Gyr. It is interesting to observe that although gas accretion onto the central galaxy has already stopped at  $z \sim 4$ , when  $M_{\text{halo}} \sim 10^{11} h^{-1} M_{\odot}$ , the accretion of cold gas in substructures along the filaments continue to be important until  $z \sim 2$ , when  $M_{\text{halo}} \sim 10^{12} h^{-1} M_{\odot}$ . Semianalytic models of galaxy formation explain the galaxy bimodality with the shutdown star formation in haloes above a critical mass  $M_{\text{crit}}$ . Our work partly explains why these studies find the best fit to the data for  $M_{\text{crit}} \simeq 2 \times 10^{12} M_{\odot}$  (e.g. Cattaneo et al. 2006) despite the fact that a purely theoretical analytic approach gives a shutdown mass for the disruption of cold filaments of  $\sim 3 \times 10^{11} M_{\odot}$  (Dekel & Birnboim 2006). In conclusion, Fig. 6 and Fig. 7 show that, without refuelling by gas-rich mergers or cooling flows, the central galaxy is already on its way to getting ‘red and dead’ at  $z \sim 2.5$ . That occurs because shock heating rearranges the gas in the cold filaments into a hot static spherical halo (Fig. 4). Without merging or cooling flows our galaxy would simply evolve into a red early-type spiral galaxy with  $M_{\text{star}} \sim 1 - 2 \times 10^{11} h^{-1} M_{\odot}$ .

Mergers cause galaxies to evolve toward earlier type morphologies but at the same time they reactivate star formation. In fact, mergers are the dominant mechanism in supplying cold gas to the galaxy after the accretion of cold filamentary flows has ceased. We caution that this may be partly due to our artificially long cooling time, which derives from computing radiative cooling for primordial metal abundances. Our cosmological simulations support the earlier conclusion derived by Springel et al. (2005b) in the case of isolated mergers: mergers cannot form *red* elliptical galaxies unless there is a quenching mechanism that prevents them from leaving tails of star formation inconsistent with the red colours of elliptical galaxies (e.g. Springel et al. 2005b). Our simulations show that the model without AGN feedback fails to form a convincing elliptical galaxy. In the simulation without black hole, the galaxy ends up with a visual appearance and a Sersic index ( $n \simeq 2.5$ ) consistent with those of an elliptical galaxy. It also has boxy isophotes. However, it has a central blue light excess that is abnormal for a galaxy with these properties and that places it squarely on the blue sequence (Fig. 10).

In contrast, already  $\sim 1\%$  of the energy released by the growth of a supermassive black hole is sufficient to quench star formation in galaxy mergers if it can be coupled effectively with the surrounding gas. This claim is motivated by considering that our black hole has accreted a mass that is  $\sim 5$  times lower than the typical mass of the central black hole in an elliptical galaxy with  $M_{\text{star}} \sim 10^{11} h^{-1} M_{\odot}$ . Therefore, the same energy that we extract with  $\beta = 0.05$  could have been extracted with a lower heating efficiency but a larger mass growth. The limited growth of the black hole is due to the promptness of AGN feedback, which immediately blows away the fuel for accretion as soon as the accretion starts. We believe that the lower growth in our cosmological simulation with respect to the growth of black holes in simulations of isolated mergers is partly a resolution effect, which causes the energy injection to be smoothed over a larger part of the galaxy. In simulations of isolated mergers, outflows are primarily affecting the central region, and

therefore they do not have the same immediate effect on gas at larger radii, which may be about to fall onto the black holes.

Our simulation with AGN feedback forms a galaxy that is already red after  $z \sim 0.6$  and that is perfectly on the red sequence at  $z = 0$  (Fig. 10) consistently with its elliptical morphology. The suppression of star formation, which has moved the galaxy to the red sequence, is due to the combination of two physical phenomena: the shutdown of cold mode accretion by shock heating, and AGN feedback quenching star formation in galaxy mergers. AGN feedback also contributes to raising the entropy of the hot IGM by removing low entropy tails vulnerable to developing cooling flows.

AGN activity appears to be directly connected with merging. The two times when the black hole reaches the Eddington limit ( $M_B \sim -22.6$  and  $M_B \sim -23$ ) coincide with the two major mergers at  $z \simeq 2.04$  and  $z \simeq 0.075$ . We also find AGN activity without us being able to observe an ongoing merger ( $z \simeq 0.63$ ), but, even in these cases, we see morphological disturbances and tidal features, which can be traced to the interaction with small companions. It is in fact an episode of this kind that shuts down the residual star formation activity at  $z \simeq 0.63$  and moves the galaxy from the blue to the red sequence. This episode supports the observational notion that AGN host galaxies are transition objects in migration from the blue to the red sequence (Graves et al. 2007; Schawinski et al. 2007), although we also see a transition in the properties of AGN hosts from blue and star-forming at  $z \sim 2$  to red and dead at  $z \sim 0$  (Fig. 7). This trend is in agreement with observational results, which find that the hosts of low redshift AGNs are mainly on the red sequence or on the top of the blue cloud (Kauffmann et al. 2003b; Jahnke et al. 2004a; Sánchez et al. 2004; Nandra et al. 2007), while at high redshift the observations support a connection between AGN activity and star formation (Jahnke et al. 2004b). The black hole accretion event at  $z \sim 0.1$  is significant because it shows an example of an  $M_B \sim -23$  AGN in a red ( $U - V \sim 1.2$ ) boxy elliptical with a Sersic index of  $n \simeq 6.8$ . One should not be puzzled by the fact that one of the two most important episodes of luminous accretion is happening at such a low redshift because we have simulated the formation of an intermediate mass elliptical in a halo that has just passed the critical mass for star formation shutdown. Therefore it is not surprising that this galaxy is hosting Seyfert activity at low redshift. Had we simulated the central galaxy of a galaxy cluster, where the critical halo mass is crossed much earlier, we would have seen a much more luminous AGN and a shutdown of AGN activity at a much higher redshift. This is directly related to the downsizing of galaxy formation (Cattaneo et al., in preparation).

Our simulations contain metal enrichment of the ISM by supernovae. We have found that even moderate AGN winds can easily produce the required enrichment of the IGM at  $z \sim 3$  although in realistic situations supernova winds are also likely to play a role (Springel & Hernquist 2003). The field of studying the complex interaction between galaxy formation, AGNs and the ISM is still in its infancy. However, the need for AGN feedback in galaxy formation appears as a fundamental physical results independently of the many uncertainties concerning the details of how it works.

## ACKNOWLEDGMENTS

We are grateful to V. Springel for providing the GADGET-2 code used for this study. We also thank G. Yepes and M. Hoeft for useful conversations.

Generating the initial conditions was done at the NIC in Jülich. The simulations without black hole were performed on the MareNostrum supercomputer at the BSC in Barcelona. The rest of the simulations were done on the HLBR II SGI's Altix 4700 platform at the LRZ in Garching.

## REFERENCES

- Baldry I. K., Balogh M. L., Bower R. G., Glazebrook K., Nichol R. C., Bamford S. P., Budavari T., 2006, MNRAS, 373, 469
- Bell E. F., Wolf C., Meisenheimer K., Rix H., Borch A., Dye S., Kleinheinrich M., Wisotzki L., McIntosh D. H., 2004, ApJ, 608, 752
- Best P. N., Kaiser C. R., Heckman T. M., Kauffmann G., 2006, MNRAS, 368, L67
- Bondi H., 1952, MNRAS, 112, 195
- Bower R. G., Benson A. J., Malbon R., Helly J. C., Frenk C. S., Baugh C. M., Cole S., Lacey C. G., 2006, MNRAS, 370, 645
- Bruzual G., Charlot S., 2003, MNRAS, 344, 1000
- Cattaneo A., Bernardi M., 2003, MNRAS, 344, 45
- Cattaneo A., Blaizot J., Weinberg D. H., Colombi S., Dave R., Devriendt J., Guiderdoni B., Katz N., Keres D., 2007, pre-print astro-ph/0605750
- Cattaneo A., Combes F., Colombi S., Bertin E., Melchior A.-L., 2005a, MNRAS, 359, 1237
- Cattaneo A., Combes F., Colombi S., Bertin E., Melchior A.-L., 2005b, MNRAS, 359, 1237
- Cattaneo A., Dekel A., Devriendt J., Guiderdoni B., Blaizot J., 2006, MNRAS, 370, 1651
- Cattaneo A., Teyssier R., 2007, MNRAS, 376, 1547
- Ciotti L., Ostriker J. P., 2007, ApJ, 665, 1038
- Contardo G., Steinmetz M., Fritze-v. Alvensleben U., 1998, ApJ, 507, 497
- Croton D. J., Springel V., White S. D. M., De Lucia G., Frenk C. S., Gao L., Jenkins A., Kauffmann G., Navarro J. F., Yoshida N., 2006, MNRAS, 365, 11
- Cuadra J., Nayakshin S., Springel V., di Matteo T., 2006, MNRAS, 366, 358
- Dekel A., Birnboim Y., 2006, MNRAS, 368, 2
- Di Matteo T., Springel V., Hernquist L., 2005, Nature, 433, 604
- Dunn R. J. H., Fabian A. C., 2006, MNRAS, 373, 959
- Fabian A. C., 1999, MNRAS, 308, L39
- Fabian A. C., Celotti A., Blundell K. M., Kassim N. E., Perley R. A., 2002, MNRAS, 331, 369
- Fabian A. C., Sanders J. S., Allen S. W., Crawford C. S., Iwasawa K., Johnstone R. M., Schmidt R. W., Taylor G. B., 2003, MNRAS, 344, L43
- Fabian A. C., Sanders J. S., Taylor G. B., Allen S. W., Crawford C. S., Johnstone R. M., Iwasawa K., 2006, MNRAS, 366, 417
- Ferrarese L., Merritt D., 2000, ApJL, 539, L9



- Forman W., Nulsen P., Heinz S., Owen F., Eilek J., Vikhlinin A., Markevitch M., Kraft R., Churazov E., Jones C., 2005, *ApJ*, 635, 894
- Häring N., Rix H., 2004, *ApJL*, 604, L89
- Haardt F., Madau P., 1996, *ApJ*, 461, 20
- Hopkins P. F., Bundy K., Hernquist L., Ellis R. S., 2007, *ApJ*, 659, 976
- Hopkins P. F., Hernquist L., Cox T. J., Robertson B., Di Matteo T., Springel V., 2006, *ApJ*, 639, 700
- Hopkins P. F., Hernquist L., Martini P., Cox T. J., Robertson B., Di Matteo T., Springel V., 2005, *ApJL*, 625, L71
- Jahnke K., Kuhlbrodt B., Wisotzki L., 2004, *MNRAS*, 352, 399
- Jahnke K., Sánchez S. F., Wisotzki L., Barden M., Beckwith S. V. W., Bell E. F., Borch A., Caldwell J. A. R., Häussler B., Heymans C., Jogee S., McIntosh D. H., Meisenheimer K., Peng C. Y., Rix H.-W., Somerville R. S., Wolf C., 2004, *ApJ*, 614, 568
- Katz N., Weinberg D. H., Hernquist L., 1996, *ApJS*, 105, 19
- Kauffmann G., Heckman T. M., Tremonti C., Brinchmann J., Charlot S., White S. D. M., Ridgway S. E., Brinkmann J., Fukugita M., Hall P. B., Ivezić Ž., Richards G. T., Schneider D. P., 2003a, *MNRAS*, 346, 1055
- Kauffmann G., Heckman T. M., Tremonti C., Brinchmann J., Charlot S., White S. D. M., Ridgway S. E., Brinkmann J., Fukugita M., Hall P. B., Ivezić Ž., Richards G. T., Schneider D. P., 2003b, *MNRAS*, 346, 1055
- Kauffmann G., White S. D. M., Heckman T. M., Ménard B., Brinchmann J., Charlot S., Tremonti C., Brinkmann J., 2004, *MNRAS*, 353, 713
- Kennicutt Jr. R. C., 1998, *ApJ*, 498, 541
- Kereš D., Katz N., Weinberg D. H., Davé R., 2005, *MNRAS*, 363, 2
- King A., 2003, *ApJL*, 596, L27
- Klypin A., Gottlöber S., Kravtsov A. V., Khokhlov A. M., 1999, *ApJ*, 516, 530
- Klypin A., Kravtsov A. V., Bullock J. S., Primack J. R., 2001, *ApJ*, 554, 903
- Li Y., Hernquist L., Robertson B., Cox T. J., Hopkins P. F., Springel V., Gao L., Di Matteo T., Zentner A. R., Jenkins A., Yoshida N., 2007, *ApJ*, 665, 187
- Magorrian J., Tremaine S., Richstone D., Bender R., Bower G., Dressler A., Faber S. M., Gebhardt K., Green R., Grillmair C., Kormendy J., Lauer T., 1998, *AJ*, 115, 2285
- Marconi A., Hunt L. K., 2003, *ApJL*, 589, L21
- Maulbetsch C., Avila-Reese V., Colin P., Gottloeber S., Khalatyan A., Steinmetz M., 2007, *ApJ*
- McKee C. F., Ostriker J. P., 1977, *ApJ*, 218, 148
- McLure R. J., Jarvis M. J., Targett T. A., Dunlop J. S., Best P. N., 2006, *MNRAS*, 368, 1395
- Meza A., Navarro J. F., Steinmetz M., Eke V. R., 2003, *ApJ*, 590, 619
- Murray N., Quataert E., Thompson T. A., 2005, *ApJ*, 618, 569
- Naab T., Johansson P. H., Ostriker J. P., Efstathiou G., 2007, *ApJ*, 658, 710
- Nandra K., Georgakakis A., Willmer C. N. A., Cooper M. C., Croton D. J., Davis M., Faber S. M., Koo D. C., Laird E. S., Newman J. A., 2007, *ApJL*, 660, L11
- Navarro J. F., Benz W., 1991, *ApJ*, 380, 320
- Navarro J. F., Steinmetz M., 1997, *ApJ*, 478, 13
- Peng C. Y., Ho L. C., Impey C. D., Rix H.-W., 2002, *AJ*, 124, 266
- Peng C. Y., Impey C. D., Rix H.-W., Kochanek C. S., Keeton C. R., Falco E. E., Lehár J., McLeod B. A., 2006, *ApJ*, 649, 616
- Power C., Navarro J. F., Jenkins A., Frenk C. S., White S. D. M., Springel V., Stadel J., Quinn T., 2003, *MNRAS*, 338, 14
- Rafferty D. A., McNamara B. R., Nulsen P. E. J., Wise M. W., 2006, *ApJ*, 652, 216
- Sánchez S. F., Jahnke K., Wisotzki L., McIntosh D. H., Bell E. F., Barden M., Beckwith S. V. W., Borch A., Caldwell J. A. R., Häussler B., Jogee S., Meisenheimer K., Peng C. Y., Rix H.-W., Somerville R. S., Wolf C., 2004, *ApJ*, 614, 586
- Scannapieco E., Oh S. P., 2004, *ApJ*, 608, 62
- Schaye J., Aguirre A., Kim T.-S., Theuns T., Rauch M., Sargent W. L. W., 2003, *ApJ*, 596, 768
- Silk J., Rees M. J., 1998, *A&A*, 331, L1
- Springel V., 2005, *MNRAS*, 364, 1105
- Springel V., Di Matteo T., Hernquist L., 2005a, *ApJL*, 620, L79
- Springel V., Di Matteo T., Hernquist L., 2005b, *ApJL*, 620, L79
- Springel V., Di Matteo T., Hernquist L., 2005c, *MNRAS*, 361, 776
- Springel V., Hernquist L., 2003, *MNRAS*, 339, 289
- Thomas D., Maraston C., Bender R., Mendes de Oliveira C., 2005, *ApJ*, 621, 673
- Tremaine S., Gebhardt K., Bender R., Bower G., Dressler A., Faber S. M., Filippenko A. V., Green R., Grillmair C., Ho L. C., Kormendy J., Lauer T. R., Magorrian J., Pinkney J., Richstone D., 2002, *ApJ*, 574, 740
- Voit G. M., Donahue M., 2005, *ApJ*, 634, 955
- Walter F., Carilli C., Bertoldi F., Menten K., Cox P., Lo K. Y., Fan X., Strauss M. A., 2004, *ApJL*, 615, L17
- Yepes G., Kates R., Khokhlov A., Klypin A., 1997, *MNRAS*, 284, 235